Delft University of Technology

MSC Thesis

Faculty of Civil Engineering & Geosciences, TU Delft

Hydrogen Storage in Salt Caverns: Prediction of the Elasto-viscoplastic Behaviour of Rock Salt

Author:
Nordin Tippersma

December 10, 2020

Hydrogen Storage in Salt Caverns

Prediction of the Elasto-viscoplastic Behaviour of Rock Salt

by

N. Tippersma

to obtain the degree of Master of Science
at the Delft University of Technology,
to be defended publicly on Friday December 18, 2020 at 13:15 PM.

Student number:	4468996	
Project duration:	November 1, 2019 – December 18, 2020	
Advisor:	Associate Prof. Hadi Hajibeygi,	CITG, TU Delft
Other committee members:	Prof. Giovanni Bertotti,	CITG, TU Delft
	Associate Prof. Phil Vardon,	CITG, TU Delft
	Associate Prof. Annemarie Muntendam-Bos,	CITG, TU Delft

TUDelft

Abstract

A transition towards more renewable energy sources such as wind- and solar energy is underway. These sources can be unpredictable with regard to energy production and therefore energy storage has become a major concern. A promising technique, Underground Hydrogen Storage (UHS), converts excess energy into hydrogen and stores it underground, after which, by reversing the process, the stored energy can be used when the imbalance between supply and demand is great. Hydrogen storage in salt caverns is particularly attractive because of their high sealing capacity, low amount of cushion required, the inert nature of rock salt and high possible injection and withdrawal rates. For energy storage purposes, these salt caverns are exposed to different cyclic loading conditions during operation, resulting in variations in stress in and around the cavern. Investigation of the mechanical response of rock salt under cyclic loading conditions is essential for the safety assessment and usability of the cavern. The response of the system to varying loading conditions can be mainly divided into two groups, either time-dependent or stress-dependent. The main focus of this thesis is to record the stress-dependent behaviour of rock salt under varying loading conditions. More specifically, it focuses on nonlinearity that occurs due to viscoplasticity. This phenomenon can be described as the rate-dependent behaviour of a material that occurs when a material exceeds a certain stress level, after which irreversible deformation occurs. This thesis describes the development of a 2D FEM (finite element method) simulator on an unstructured grid that captures the mechanical response. To model the stress-dependent behaviour, the viscoplastic model proposed by Desai is used. This model is based on the non-associated flow rule and takes into account material dilatancy and compressibility. In addition, the model allows for hardening, the tensile strength of rock salt and variation in yield behaviour with pressure variation. Sonar data from cavern EPE S43 is utilised to test the simulator. This case showed that irreversible deformation occurs as a result of the stress-dependent behaviour of rock salt. For this specific cavern, the total working volume of the cavern decreased roughly by 0.0003% over three operating cycles, indicating that viscoplastic deformation itself does not pose significant risks to the cyclic storage of hydrogen in salt caverns.

Contents

List of Figures

List of Tables

1
Introduction

In a world in desperate need of decarbonisation, solar, wind and other renewable energy sources are the future, but our current ability to store their excess energy falls short. Integration of renewable energy sources into the electricity grid is predicted to help the European Union achieve its energy and greenhouse gas emission targets. Two critical concerns that remain are the natural fluctuation in the energy supply from renewable energy sources, such as wind and solar, and the discrepancy between energy supply and demand. That is why large-scale storage spaces are necessary to accommodate this imbalance between demand and supply.

Many options for storing energy are currently being explored, while the scalability of the techniques in terms of the amount of storage space occupied or dependence on favorable environmental factors are obstacles to overcome. The geological subsurface is seen as a medium that can provide the capacity for large-scale energy storage. Caglayan and Weber (2020) identified that underground hydrogen storage (UHS), a technique that converts energy into hydrogen through electrolysis, can serve as a feasible and flexible solution.

$$2H_2O(\mathrm{l}) + \text{energy} \longrightarrow 2H_2(\mathrm{g}) + O_2(\mathrm{g}) \tag{1.1}$$

Renewable energy sources can provide the energy to convert water into hydrogen and by reversing the process, the stored energy can be used when the imbalance between supply and demand is great. Compared to air, hydrogen has a higher energy density, which means that hydrogen atoms can store more energy under comparable conditions (Kabuth and Dahmke, 2017).

1.1. Potential of Hydrogen Storage

The three most suitable options for underground hydrogen storage are aquifers, depleted hydrocarbon reservoirs and salt caverns. Hydrogen storage in salt caverns is particularly attractive due to their high sealing capacity, low amount of cushion gas required, the inert nature of rock salt and high possible injection and withdrawal rates. In the past, hydrogen has already been successfully stored in caverns for various applications. For example, hydrogen was stored in the Clemens Salt Dome, Texas (US) by ConocoPhillips and Praxair (Hévin, 2019). The knowledge gained from these experiences can easily be transferred to this industry.

Rock salt occurs underground under natural conditions and is mainly composed of halite crystals with small amounts of anhydrite, polyhalite, clay and silt. Through salt mining, some of these caverns already exist. Due to the solubility of salt in water, other caverns can be created by pumping water into the formation, a technique called "leaching". An estimate of the potential for underground energy storage for the Netherlands has been carried out by Juez-Larré and van Gessel (2019). This study includes the potential of hydrogen storage in salt caverns. In total, approximately 321 caverns can be constructed with a storage capacity of 14.5 billion m^3 of hydrogen (corresponding energy content 43 TWh). In perspective, the total energy consumption in the Netherlands in 2018 was about 860 TWh (EBN, 2018), which means that storage in salt caverns on land only covers five percent of the total energy consumption in the country. This means that this method will mainly be used to absorb peaks in energy demand.

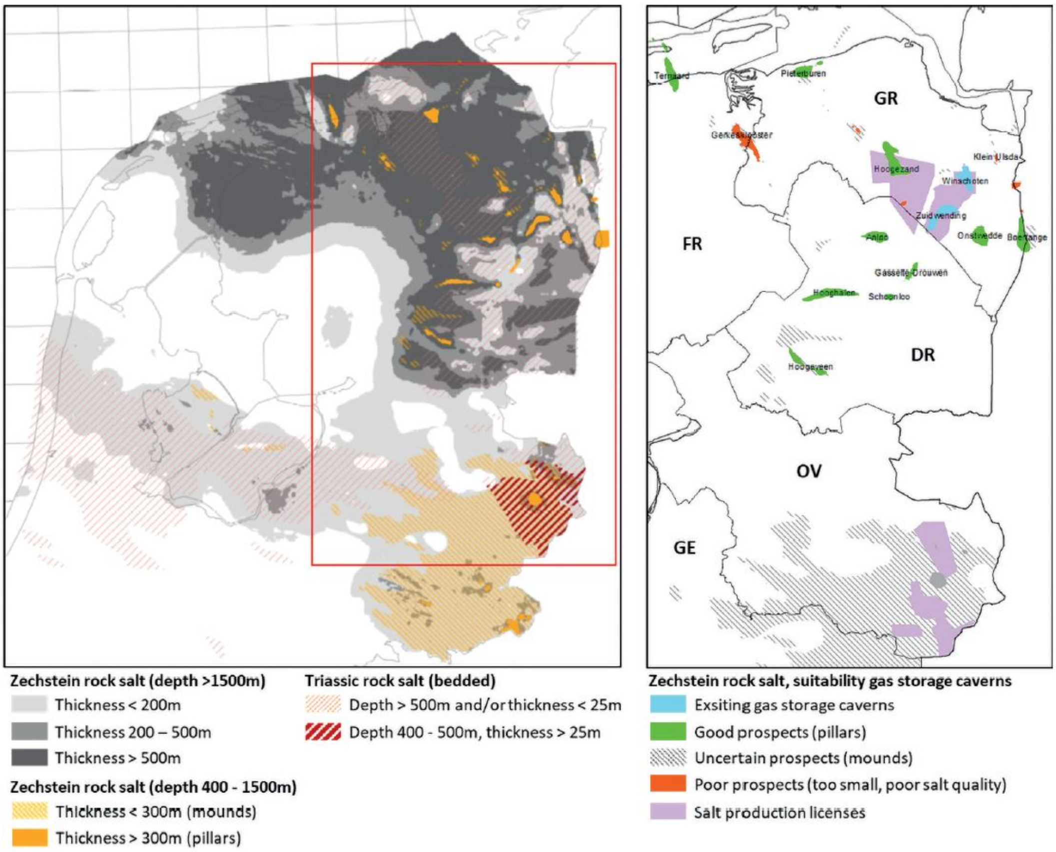

Figure 1.1: Distribution of Zechstein and Triassic formation in the Netherlands (left) and the suitability of gas storage in the northern provinces (right) (from Juez-Larré and van Gessel (2019)).

For energy storage purposes, these salt caverns are exposed to different cyclic loading conditions during operation, resulting in variations in stress in and around the cavern. Investigation of the mechanical response of the rock salt under these varying conditions is essential for safety assessment and usability of the cavern. Prediction of the behaviour can be made through simulation, which provides a numerical solution of the equations describing the physical processes of interest on a mesh that represents the control volume of interest and mimics the behaviour of the real system. The response of the system due to the varying loading conditions can be mainly divided into two groups, either time-dependent or stress-dependent. The main focus of this thesis is to record the stress-dependent behaviour of rock salt under varying loading conditions.

1.2. Previous Work

The stress-deformation response of natural rock salt can be very complex. Herrmann and Wawersik (1980) noted that among many factors that significantly influence rock salt behaviour are pressure, deviatoric stress, time, temperature and loading path. At low confinement pressures, it fails in a brittle way but becomes more and more plastic at higher pressures.
Several researchers have proposed models that can capture the stress-dependent behaviour based on Perzyna's theory of viscoplasticity (Perzyna, 1966), which vary according to their assumptions, the number of model parameters and their complexity. Perzyna decomposed the total strain into an elastic and inelastic component. The inelastic or plastic component represents the combined viscous and plastic effects. In this model, the plastic strain refers to a specific flow function. This function usually depends on the current state of stress and on one or more state variables which include the loading history.

Various yield functions have been used in the past. Zienkiewicz and Cormeau (1974) and Cormeau and Zienkiewicz (2005) used different classical yield criteria for plasticity, Katona and Mulert (1984) and Baladi and Rohani (1983) used the cap model. In this thesis a generalized yield function proposed by Desai (Desai (1980), Faruque (1985), Desai and Zhang (1987), Desai and Salami (1987), Desai and Varadarajan (1987), Desai and Laloui (1997)) is used. The advantage of this yield function is that it captures plastic deformation in a single continuous yield surface. Based on a non-associated flow rule, this model takes material dilatancy and compressibility into account, improving the fit to experimental data. Moreover, the model allows for hardening, tensile strength of rock salt and variation in yield behaviour with variation in pressure. Compared to other models, it has a low number of model parameters, including physical meaning. The model precludes temperature or time-dependent creep effects that can occur during the simulation duration.

1.3. Thesis Outline

This thesis is intended to guide the reader through the whole procedure of implementing the chosen model in numerical simulation. The theory, chapter 2, discusses the entire theoretical foundation on which the simulator is built. Chapter 3 deals with the description of parameters followed by the procedure of implementing the model into finite element code. The simulation results are presented in chapter 4. A discussion of the simulation results and the main conclusion followed by possible improvements of the study are given in chapter 5.

2

Theory

This chapter covers the theoretical basis on which the model is built. First, an elaboration of the problem to be solved is discussed, accompanied by the assumptions made. Second, the governing equations to solve the problem will be introduced. Third, it explains the principle of minimum potential energy that is used to derive the finite element equations. Finally, the viscoplastic formulation of the model is examined. The implementation of these equations will be discussed in the following chapters.

2.1. Problem Statement

In order to apply this storage technique on a large scale, understanding the mechanical response of the cavern is paramount for safety assessment and serviceability. During use, these caverns can be depleted and filled on a daily to monthly basis, resulting in rapid changes in stress in and around the cavern.

To describe how a material responds to externally applied loads, two commonly used definitions are 'stress' and 'strain'. Stress (σ) is commonly referred to as a quantity that describes the distribution of a body's internal forces. Strain (ε) is often used to quantify the deformation that occurs in a body. The concepts of stress and strain are closely related. The relationship between the two can be described with the help of a stress-strain diagram (fig.2.1).

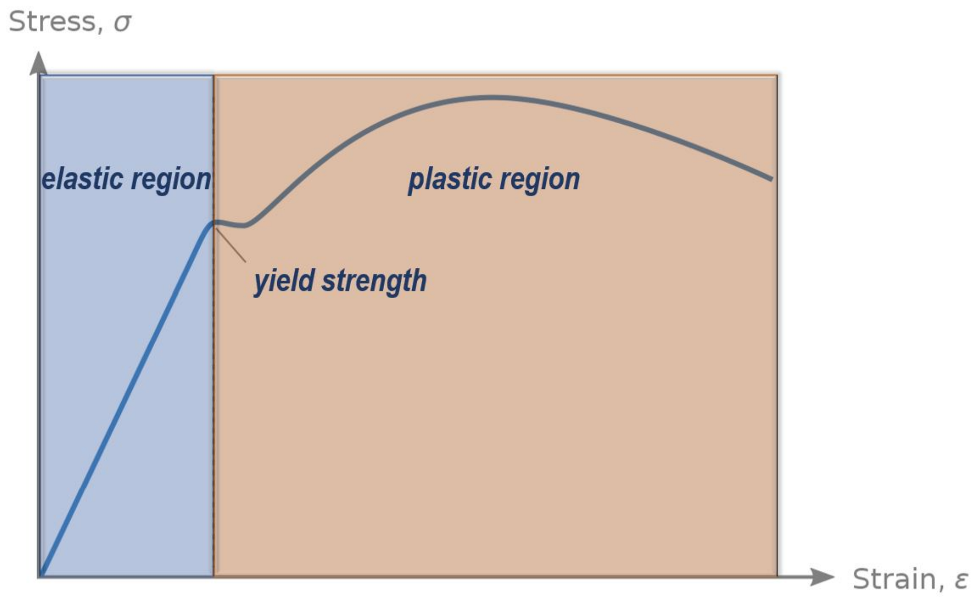

Figure 2.1: Example of a stress-strain diagram visualizing both the elastic and plastic region for a brittle material.

Stress and strain can be calculated (or measured) when a force is applied to the material. Within the elastic region, the relationship between stress and strain is linear. Any deformation that occurs in this area is completely reversed when the load is removed. In the plastic region, the relationship between stress and strain is no longer linear. Deformation is not reversed when the load is removed and there is permanent plastic deformation.

For many materials, it is known how to model the response of the material in the elastic region, although modelling of the behaviour in the plastic region remains complex. In solid mechanics, it has become common practice to separate the two main groups of phenomena described by “creep” and “(visco)plasticity”. The first includes all-time effects and results in creep strains. The second group develops permanent (plastic) strains instantaneously and time does not play a direct role.

2.1.1. Objectives

This thesis focuses mainly on nonlinearity that occurs as a result of viscoplasticity (e.g. the second group). The general definition used for that behaviour is that viscoplasticity describes the rate-dependent behaviour of a material that occurs when a material exceeds a certain stress level (the yield strength), after which irreversible deformation occurs. The model used will combine both the theory of linear elasticity and theory of plasticity to describe the response of the material. In order to model this process, the simulator should be able to predict:

- The stress and strain state of rock salt in the elastic region under monotonically increasing pressure conditions.
- The viscoplastic behaviour of rock salt in the plastic region under monotonically increasing pressure conditions.
- The transition (yield point) between the elastic and plastic region.
- The elastic and viscoplastic behaviour under cyclic loading conditions.

2.1.2. Assumptions

To develop a model capable of capturing these macroscopic features, the following assumptions are made:

- The problem under investigation is a 2D plane strain problem
- The material is isotropic and homogeneous
- Deformations are assumed to be small so small strain theory holds (eq. 2.17)
- Adiabatic conditions apply (no heat transfer)
- The cavern is instantly excavated and in equilibrium at the start (t=0) of the model and any prior deformation or deterioration has not been accounted for.
- Material parameters remain constant through simulation procedure unless stated otherwise.
- Continuity of the body is assumed (eg. 2.10 & 2.11) (i.e. no cracks or overlapping parts)

2.2. Governing Equations

The next two sections are mainly based on the books of Rao (2005) and Pepper and Heinrich (2017) which describe in detail the equations used.

2.2.1. Introduction

The degree of deformation that occurs on a particular body under specific load conditions (F), as shown in figure 2.2, cannot be directly determined. First, the distribution of displacements in the body must be calculated. Then stresses and strains can be calculated from the displacement field.

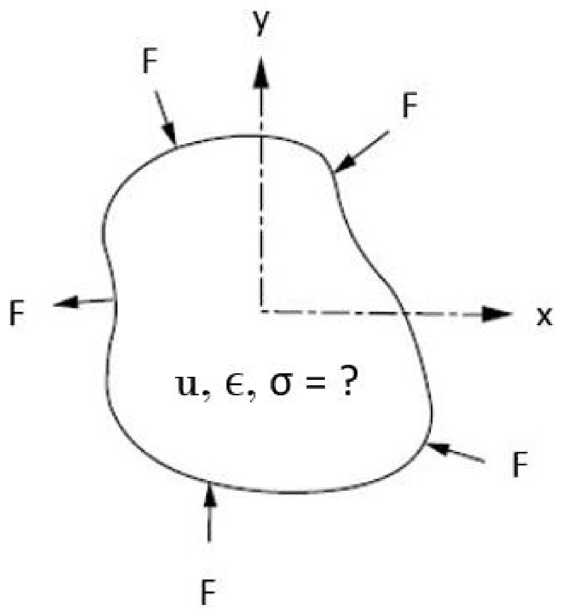

Figure 2.2: Arbitrary body under load conditions for which the distribution of displacements (u), strain (ε) and stress (σ) are unknown (adapted from Rao (2005)).

Following this procedure, there are eight unknown quantities for the given problem. So, it takes eight equations to solve the problem; two equilibrium equations, three stress-strain relationships and three strain-displacement relationships. The unknown quantities for this problem are given in table 2.1.

Table 2.1: Unknown quantities for the given problem.

Unknowns	2D
Displacements	u, v
Stresses	σ_{xx}, σ_{yy}, σ_{xy}
Strains	ε_{xx}, ε_{yy}, ε_{xy}
Total number of unknowns	8

In addition, some extra equations must be satisfied to constrain the problem (compatibility equations and boundary conditions). The equations to solve are discussed in the following sections, starting from the momentum balance equation.

2.2.2. Equilibrium condition

The momentum balance equation for the given problem can be described as:

$$\nabla \cdot \vec{\sigma} = -\vec{f} \tag{2.1}$$

where ∇ denotes the divergence operator, σ the stress tensor and f the force vector. If the body is in equilibrium, which means that the net force acting on the body is zero, then in 2D the equilibrium state can be represented as:

$$\frac{\partial \sigma_{xx}}{\partial x} + \frac{\partial \sigma_{xy}}{\partial y} + f_x = 0 \tag{2.2}$$

$$\frac{\partial \sigma_{xy}}{\partial x} + \frac{\partial \sigma_{yy}}{\partial y} + f_y = 0 \tag{2.3}$$

in which σ_{ij} indicates stress in either x, y or xy direction, f_x and f_y denote the force applied in either x or y direction.

2.2.3. Stress-strain relations

For a linear elastic body, stress and strain can be related by using Hooke's law. For a 2D plane strain problem, Hooke's law is described as:

$$\vec{\sigma} = [D]\vec{\varepsilon} \tag{2.4}$$

in which σ is the stress, ε the strain and [D] is the elasticity tensor which can be written in terms of the Young's modulus (E) and the Poisson's ratio (v) of the material under investigation:

$$D = \frac{E}{(1+v)(1-2v)}\begin{bmatrix} 1-v & v & 0 \\ v & 1-v & 0 \\ 0 & 0 & \frac{1-2v}{2} \end{bmatrix} \tag{2.5}$$

The component of stress in z-direction will be nonzero and is given by:

$$\sigma_{zz} = v(\sigma_{xx} + \sigma_{yy}) \tag{2.6}$$

2.2.4. Strain-displacement relations

To relate strain and displacement, the following three equations are used:

$$\varepsilon_{xx} = \frac{\partial u}{\partial x} \tag{2.7}$$

$$\varepsilon_{yy} = \frac{\partial v}{\partial y} \tag{2.8}$$

$$\varepsilon_{xy} = \frac{\partial u}{\partial y} + \frac{\partial v}{\partial x} \tag{2.9}$$

where ε is the strain in the given direction, u and v the displacement in x and y directions, respectively.

2.2.5. Closing Relations

The next two equations, called compatibility equations, ensure that the body is continuous before and after deformation. In short, this means that there are no cracks in the body after deformation and that no parts overlap. The equations can be summarized according to Rao (2005) as:

$$\frac{\partial^2 \varepsilon_{xx}}{\partial y^2} + \frac{\partial^2 \varepsilon_{yy}}{\partial x^2} = \frac{\partial^2 \varepsilon_{xy}}{\partial x \partial y} \tag{2.10}$$

$$\frac{\partial^2 \varepsilon_{zz}}{\partial y^2} = \frac{\partial^2 \varepsilon_{zz}}{\partial x^2} = \frac{\partial^2 \varepsilon_{zz}}{\partial x \partial y} = 0 \tag{2.11}$$

Finally, the last constraints required are boundary conditions. These conditions will be discussed in more detail in a subsequent chapter.

2.3. Principle of Minimum Potential Energy

To discretize the given problem in finite element equations, two approaches can be used, either the differential equation formulation (Galerkin approach) or the variational formulation (Rayleigh-Ritz approach). In continuum mechanics, a variational formulation approach is often used and therefore such a formulation in the form of the principle of minimum potential energy is applied.

The potential energy of a body (π_p) can be defined as:

$$\pi_p = \pi - W_p \tag{2.12}$$

where π is the strain energy density, and W_p the work done on the body by external forces. If the potential energy, π_p, is expressed in terms of displacements u, v (2D), the principle of minimum potential energy at equilibrium state is:

$$\delta\pi_p(u, v) = \delta\pi(u, v) - \delta W_p(u, v) = 0 \tag{2.13}$$

Since the problem of plane strain is studied, assuming constant thickness, the strain energy density of a linear elastic body can be defined as:

$$\pi = \frac{1}{2}\int\int_A \vec{\varepsilon}^T \vec{\sigma} t dA \tag{2.14}$$

where ε^T is the transpose of the strain vector, t the thickness of the body and A the area of the body. Using Hooke's law describing the stress-strain relationship as follows:

$$\vec{\sigma} = [D]\vec{\varepsilon} \tag{2.15}$$

Substituting Hooke's law in the strain energy density equation results in:

$$\pi = \frac{1}{2}\int\int_A \vec{\varepsilon}^T D \vec{\varepsilon} t dA \tag{2.16}$$

Under the assumption of infinitely small strains, it is possible to divide the total strain (ε^{tot}) into an elastic (ε^{el}) and viscoplastic component (ε^{vp}), such that:

$$\overrightarrow{\varepsilon^{tot}} = \overrightarrow{\varepsilon^{el}} + \overrightarrow{\varepsilon^{vp}} \tag{2.17}$$

Since the strain energy density is given for an elastic body, it can be rewritten to:

$$\overrightarrow{\varepsilon^{el}} = \overrightarrow{\varepsilon^{tot}} - \overrightarrow{\varepsilon^{vp}} \tag{2.18}$$

In the presence of viscoplastic strain, eq.2.16 is extended with an additional term that takes into account viscoplastic strain:

$$\pi = \frac{1}{2}\int\int_A \vec{\varepsilon}^T D \vec{\varepsilon} t dA - \frac{1}{2}\int\int_A \vec{\varepsilon}^T D \overrightarrow{\varepsilon^{vp}} t dA \tag{2.19}$$

The work done by external forces can be expressed as:

$$W_p = \int\int_A \vec{\phi}^T \vec{U} t \cdot dA + \int_{S_1} \vec{\Phi}^T \vec{U} \cdot dS_1 \tag{2.20}$$

where $\vec{\phi} = \begin{bmatrix} \phi_x \\ \phi_y \end{bmatrix}$ = vector of body forces, $\vec{\Phi} = \begin{bmatrix} \Phi_x \\ \Phi_y \end{bmatrix}$ = vector of prescribed forces, $\vec{U} = \begin{bmatrix} u \\ v \end{bmatrix}$ the vector of displacements and S_1 the surface on which the forces act.
Using equation 2.19 and 2.20, the potential energy of the body can be expressed as:

$$\pi_p(u,v) = \frac{1}{2}\int\int_A \vec{\varepsilon}^T D(\vec{\varepsilon} - \overrightarrow{\varepsilon^{vp}}) t dA - \int\int_A \vec{\phi}^T \vec{U} t \cdot dA - \int_{S_1} \vec{\Phi}^T \vec{U} \cdot dS_1 \tag{2.21}$$

Since the formulation of the finite element equations is a standard procedure, the implementation of the variational formulation into finite element equations is described in appendix section A.

2.4. Viscoplastic Formulation

A Perzyna-based model is used to model the viscoplastic strain component. Perzyna (1966) developed a constitutive relationship for plastic strain rate in the following form:

$$\dot{\varepsilon}^p = \frac{\langle f(\sigma,q) \rangle}{\tau} \frac{\partial f}{\partial \sigma} \tag{2.22}$$

Within this formulation, τ is the relaxation time, $\langle f(\sigma,q) \rangle$ can be thought of as the yield function, while $\frac{\partial f}{\partial \sigma}$ is the corresponding potential function (for more information about the yield and potential function see appendix section B). The bracket term is a specific case of the Macauley bracket with the following meaning:

$$\langle f(\sigma,q) \rangle = \begin{cases} 0 & \text{for } \langle f(\sigma,q) \rangle \leq 0 \\ f(\sigma,q) & \text{for } \langle f(\sigma,q) \rangle > 0 \end{cases} \tag{2.23}$$

Desai and Zhang (1987) suggested a specific yield/potential function, especially for rock salt, and modified Perzyna his formulation to:

$$\varepsilon_{ij}^{vp} = \mu_1 \left\langle \frac{F^{vp}}{F0} \right\rangle^{N_1} \frac{\partial Q^{vp}}{\partial \sigma_{ij}} \tag{2.24}$$

Within this formula, μ_1 is the fluidity parameter indicating the relative rate of plastic strain and N_1 is the stress exponent, both material parameters. F_0 is a reference value equal to one stress unit. The other functions are the yield function F^{vp} which defines the current magnitude of viscoplastic strain and the potential function $\frac{\partial Q^{vp}}{\partial \sigma_{ij}}$ which denotes the current direction of viscoplastic strain. Both functions depend on three stress invariants, the first stress invariant I_1 and the second and third deviatoric stress invariant J_2 & J_3. Stress invariants are used instead of principal stresses, as invariants do not change with different rotations of the sample (for more information on stress invariants see appendix section C).

The yield and potential function are described as follows, according to Desai and Varadarajan (1987) and Desai and Pradhan (2006):

$$F^{vp} = J_2 - \left(-\alpha \left[I_1 + 3\sigma_t \right]^n + \gamma \left[I_1 + 3\sigma_t \right]^2 \right) \left[exp^{\beta_1 I_1} - \beta cos(3\theta) \right]^{m_v} \tag{2.25}$$

$$Q^{vp} = J_2 - \left(-\alpha_q \left[I_1 + 3\sigma_t \right]^n + \gamma \left[I_1 + 3\sigma_t \right]^2 \right) \left[exp^{\beta_1 I_1} - \beta cos(3\theta) \right]^{m_v} \tag{2.26}$$

with 'θ' (commonly referred to as Lode Angle (Appendix section D)):

$$\theta = \frac{1}{3} cos^{-1} \left(\frac{-\sqrt{27} J_3}{2 J_2^{1.5}} \right) \tag{2.27}$$

Within these equations 'γ', 'β_1', 'β', 'n' & 'm_v' are material parameters (for more information on the material parameters see appendix section E). The term '$3\sigma_t$' defines the tensile rock strength of salt. The hardening parameters ('α_q' & 'α') are used to control the size of both the viscoplastic yield and potential surface in the stress space. In this thesis a simple formulation has been used to define this behaviour as:

$$\alpha = \frac{\alpha_1}{\xi^{\eta_1}} \tag{2.28}$$

where 'α_1' and 'η_1' are hardening constants and 'ξ' is the accumulated viscoplastic strain described as:

$$\xi = \int_0^t \sqrt{\varepsilon_{ij}^{vp} : \varepsilon_{ij}^{vp}} \, dt \tag{2.29}$$

The non-associative flow rule is used to define a difference between the yield and potential function and therefore 'α_q' is described as:

$$\alpha_q = \alpha + k(\alpha_0 - \alpha)(1 - \frac{\xi_v}{\xi}) \tag{2.30}$$

The parameter 'k' is a material parameter or a stress dependent function. For the sake of simplicity and brevity, it is considered constant here, similar to Desai and Zhang (1987). 'α_0' is a reference value equal to one stress unit and 'ξ_v' is the accumulated volumetric viscoplastic strain.

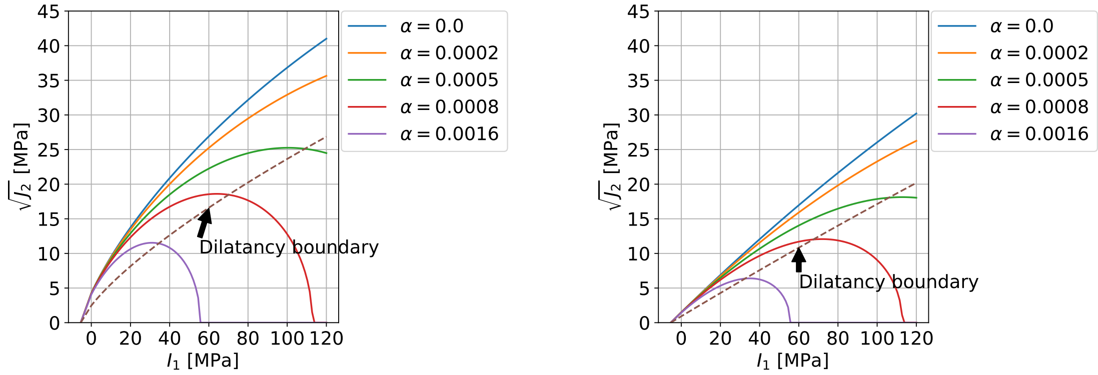

(a) (b)

Figure 2.3: Viscoplastic yield function in I_1 - $\sqrt{J_2}$ plane. (a) Evolution of viscoplastic yield function with $\theta = 60°$, compression and dilation domain are separated by the dilatancy boundary; (b) Evolution of viscoplastic yield function with $\theta = 0°$

With an increase in viscoplastic deformation, the hardening parameters decrease. This reduction is accompanied by an increase in the size of the viscoplastic yield function as can be seen in fig.2.3. The dilatancy boundary is shown for both figures, seperating the dilation domain (above) from the compressibility domain (below the boundary). The mathematical description of the dilatancy boundary can be expressed as:

$$J_2 = F^{\text{dil}}(I_1, \theta) = (1 - \frac{2}{n})\gamma I_1^2 (exp^{\beta_1 I_1} - \beta cos(3\theta))^{m_v} \left(1 + \frac{m_v \beta_1 I_1 exp(\beta_1 I_1)}{n(exp(\beta_1 I_1) - \beta cos(3\theta))}\right)^{-1} \tag{2.31}$$

2.5. Summary and Relationship to Following Sections

This research aims to develop a simulator that records the mechanical response of rock salt under stress variation. A distinction can be made between the elastic and plastic response of a material to applied loads. The plastic response consists of several components of which viscoplasticity is studied in detail in this thesis. Both the theory of elasticity and plasticity are used to describe the full response of the material.

The governing equation of the problem under study is the momentum balance equation. Moreover, the problem can be further elaborated through stress-strain and strain-displacement relationships. To discretize the system into finite element equations, the principle of minimum potential energy is used as the variational formulation.

The model proposed by Desai is used to capture the viscoplastic behaviour of the material. This model is based on the non-associated flow rule (different formulation for yield and potential function) and takes into account material dilatancy and compressibility, which improves modelling of the volumetric behaviour and improves the fit to experimental data. The model also enables hardening, the tensile strength of rock salt and variation in flow behaviour with pressure variations. Compared to other models, it has a low number of model parameters, including physical meaning. In the next chapter, the model implementation into the finite element method and the values for the model parameters are discussed.

3

Methodology

In the previous chapter, the governing equations to model the elasto-viscoplastic behaviour were discussed. In this chapter, the material parameters used in the elasto-viscoplastic model are briefly discussed. Furthermore, the implementation of the model into the finite element model is discussed. The last part of the chapter is devoted to the various test cases studied and both verification and validation of the model used.

3.1. Material Parameters

In total, the elasto-viscoplastic model used has 14 material parameters. Most of these parameters can be determined by performing laboratory tests. For the sake of brevity, an overview of the input parameters is given (Table 3.1) and a detailed description of all relevant parameters can be found in the appendix section E. Any deviation from this table will be specifically mentioned in further sections.

Table 3.1: Input material parameters for elasto-viscoplastic model.

		From Khaledi and Mahmoudi (2016a)
General Parameters	ρ_{halite}* $[\frac{\text{kg}}{\text{m}^3}]$	2160
	$\rho_{\text{overburden}}$* $[\frac{\text{kg}}{\text{m}^3}]$	2160
Elastic Parameters	K [MPa]	18,115
	μ [MPa]	9842
Viscoplastic Parameters	μ_1 [day^{-1}]	5.06e-7
	N_1	3
	n	3
	α_1 [MPa^{-1}]	0.00005
	η	0.7
	β_1 [MPa^{-1}]	4.8e-3
	β	0.995
	m_v	-0.5
	γ	0.11
	σ_t [MPa]	5.4

Parameters marked with '*' are taken from Bérest (2012).

The table is divided into three main sections; general parameters, elastic and viscoplastic parameters. The general parameters are mainly used to define the forces acting on the body. The other two sections are related to the two different regions (elastic and plastic). In principle, the elastic parameters are used to calculate the elastic strain (linear) and the viscoplastic parameters are used to define the viscoplastic strain of the given material (nonlinear).

3.2. Model Description

This section describes the workflow of the elasto-viscoplastic model. It contains the general model implemented in the finite element method and both a detailed description of the elastic predictor and plastic corrector step. The last section refers to the repository where the created source code can be found.

3.2.1. General Model

To capture the elasto-viscoplastic behaviour of the studied material, the equations from previous chapter have been integrated into an implicit scheme that updates the most important unknown displacement (u). Because the response of the system depends on the deformation history, an incremental approach between displacement and applied force is used. Quantities in the current step are denoted by a subscript 'n' while quantities from the previous step are denoted by '$n-1$'. Moreover, since viscoplastic strain depends on the current state of stress, iterative procedures must be used.

A predictor-corrector scheme is used in which the total strain increment is first calculated assuming no viscoplastic strain contribution (i.e. the model response is completely dependent on elastic strain). The output results in a stress state which is then corrected by incorporating viscoplastic strain based on the current stress state (fig.3.1). The new stresses are then updated as:

$$\sigma_n = \sigma_{n-1} + \Delta\sigma \tag{3.1}$$

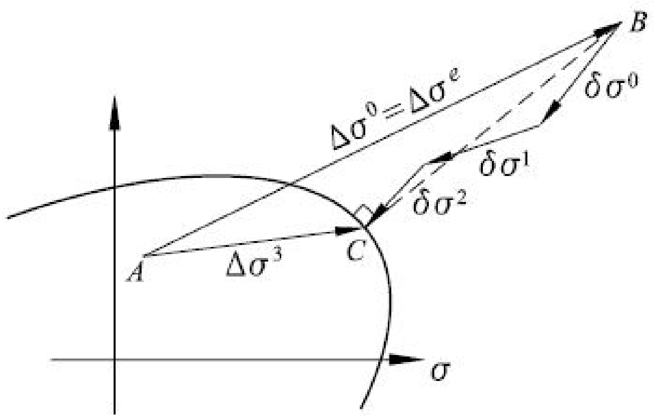

Figure 3.1: Predictor-corrector scheme in which an elastic predictor is applied from point A to B. Next, a plastic corrector is applied to return the stress state to the yield surface, point C (Krabbenhoft, 2002).

Since the output varies when including viscoplastic strains, an iterative procedure in the form of the Newton-Raphson algorithm is used to converge to the exact solution. From the formulation of finite element equations (Appendix A), the matrix notation of the problem to be solved is expressed as:

$$[K]\Delta\vec{U} = \Delta\vec{F} \tag{3.2}$$

where [K] is the stiffness matrix, $\Delta\vec{U}$ is the incremental displacement vector and $\Delta\vec{F}$ is the incremental force vector. The exact solution is obtained if the residual function (eq.3.3) is smaller than the set tolerance.

$$R_n = \Delta\vec{F_n} - [K]\Delta\vec{U_n} = 0 \tag{3.3}$$

According to the Newton-Raphson algorithm, the root of residual can be defined as follows:

$$\Delta u_n^{i+1} = \Delta u_n^i - \left\{ \left. \frac{\partial R}{\partial u} \right|_{u=\Delta u_n^i} \right\}^{-1} R(\Delta u_n^i) \tag{3.4}$$

In which $'i'$ denotes the iteration index. The derivative of the residual function with respect to displacement is described as:

$$\frac{\partial R}{\partial u} = \frac{\partial}{\partial u}\left[\Delta\vec{F_n} - [K]\Delta\vec{U_n}\right] = -[K] \tag{3.5}$$

Due to complexity, the contribution of viscoplastic strain in the force term is neglected (i.e. the derivative returns to the original stiffness matrix). Thus, the contribution of viscoplastic strain is delayed by one iteration. A flow chart with the general procedure can be found at the end of this chapter (fig.3.7), although the predictor-corrector scheme is worked out in detail first.

3.2.2. Elastic Predictor

As mentioned earlier, the elastic predictor calculates the total strain increment according to Hooke's law for linear elastic material. The input consists of two of four elastic moduli (for simplicity let's say the bulk and shear modulus), the incremental force applied, and both the density of the material and the overburden. The output of the elastic analysis is incremental displacement (Δu), incremental strain ($\Delta\varepsilon$) and incremental stress ($\Delta\sigma$). Then, the displacement, strain and stress are updated accordingly:

$$u_n = u_{n-1} + \Delta u \tag{3.6}$$

$$\varepsilon_n = \varepsilon_{n-1} + \Delta\varepsilon \tag{3.7}$$

$$\sigma_n = \Delta\sigma_{n-1} + \Delta\sigma \tag{3.8}$$

For this step no iterations are necessary. Finally, the out of plane stress (σ_{zz}) is calculated as:

$$\Delta\sigma_{zz} = (\sigma_{zz})_{n-1} + v(\Delta\sigma_{xx} + \Delta\sigma_{yy}) \tag{3.9}$$

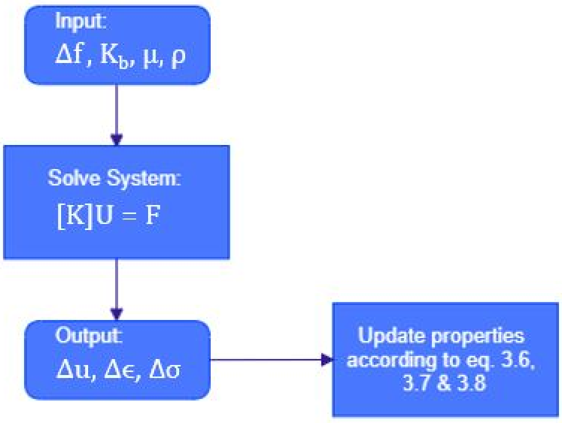

Figure 3.2: Schematic overview of the procedure for the elastic predictor.

3.2.3. Plastic Corrector

The output of the elastic predictor is used in this section as trial states. First, the stress invariants are calculated according to appendix section C. Then, the hardening parameters are calculated using equation 2.28 and 2.30. The criteria of the viscoplastic yield function are checked with the aid of the stress invariants and the hardening parameters. If $F^{vp} \leq 0$, then the stress state resides inside the viscoplastic yield function, which implies that there is no viscoplastic deformation. Hence, the response is fully elastic and can be described by Hooke's law. However, if $F^{vp} > 0$, viscoplastic deformation must be taken into account. The viscoplastic strain increment can be calculated according to eq.2.24. This equation requires the derivative of the viscoplastic potential function with respect to stress which is given by:

$$\frac{\partial Q^{vp}}{\partial\sigma} = \frac{\partial Q^{vp}}{\partial I_1}\frac{\partial I_1}{\partial\sigma} + \frac{\partial Q^{vp}}{\partial J_2}\frac{\partial J_2}{\partial\sigma} + \frac{\partial Q^{vp}}{\partial J_3}\frac{\partial J_3}{\partial\sigma} \tag{3.10}$$

Next, the Newton-Raphson algorithm is used as an iterative procedure to calculate the elastic and viscoplastic strains after which stress is updated.

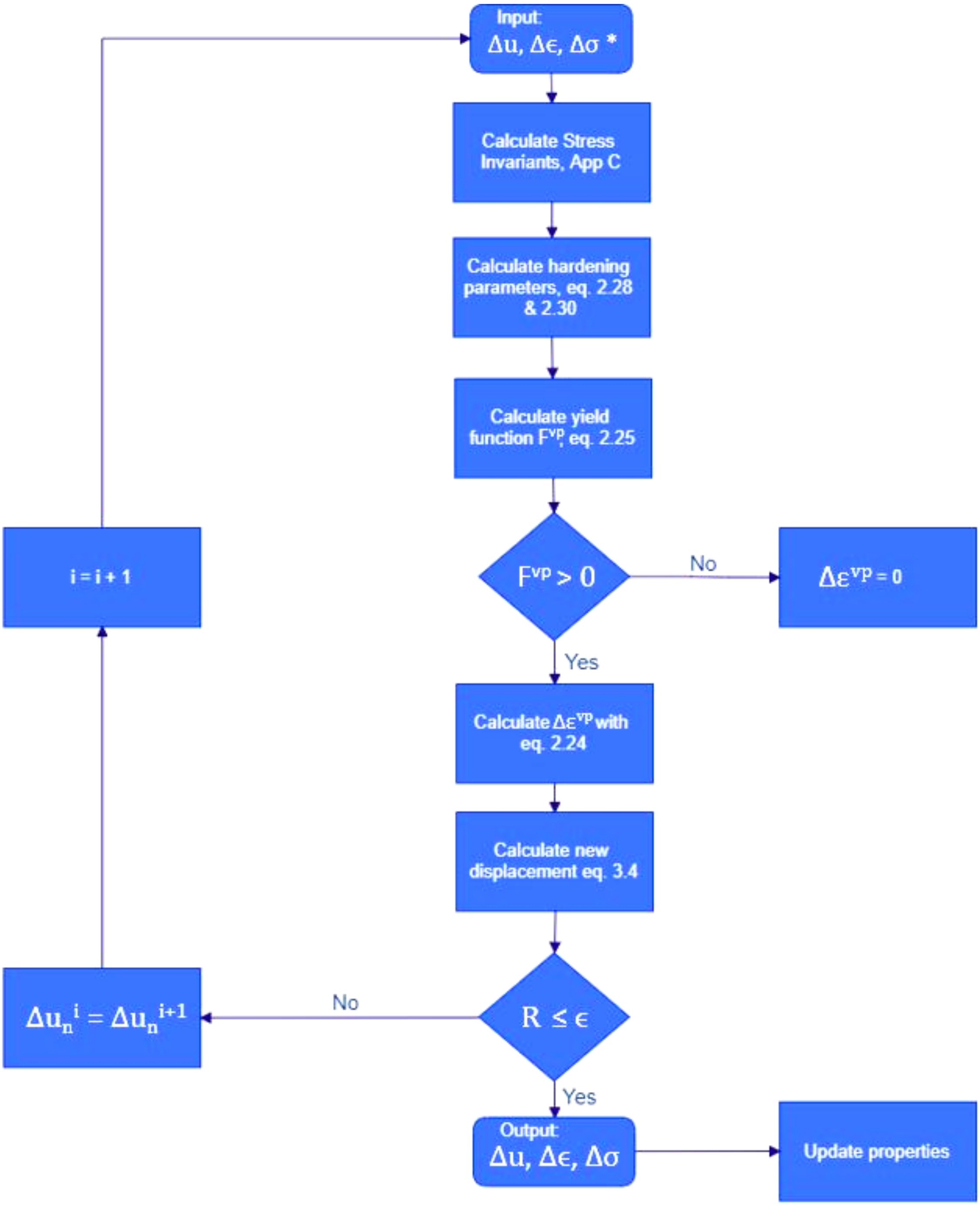

Figure 3.3: Schematic overview of the procedure for the plastic corrector in which trial states are marked with *.

3.3. Example of Test Cases

This section is dedicated to all cases tested for the elasto-viscoplastic model. Generally, three different cases are used (fig.3.4). A simple case to understand the physics of the system, also called the 'box' model case. This box represents a rectangle in which no cavity is present. Due to the simplicity of this case, the results are discussed in appendix G. The second case consists of a rectangle containing half of a cavern on the left side of the rectangle. Due to symmetry, only half of the cylindrical cave is shown. The third, and final case consists of a more naturally shaped cavern which represents an actual cavern (EPE-S43). The shape and size of the cavern is determined by sonar measurements obtained from Laban (2020) (figure I.1 & I.2). Using the open-source software 'GMSH' (*version 4.4.1*) a mesh has been created to define the domain of each case. A detailed description of how this software works is provided by Geuzaine and Remacle (2009). The dimensions of the box and cylindrical cavern are based on work of Makhmutov (2020) and are for both x and y direction ranging from -1000m to 1000m. The natural cavern case ranges in both directions from -150m to 150m. In each case the left corner point has the most negative coordinates (i.e. (-1000, -1000) or (-150, -150)). For a detailed schematic figure of each case see appendix F. The following section describes the initial and boundary conditions that are applied on these meshes.

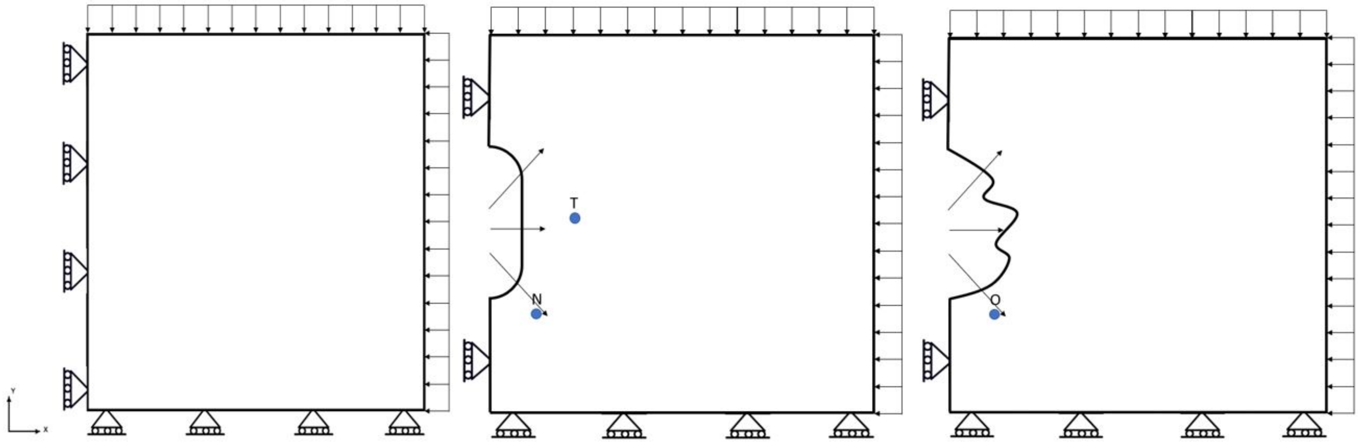

Figure 3.4: Test cases used; box case (left); cylindrical cavern including two reference points denoted by N and T (middle); natural cavern with one reference point denoted by O (right).

3.3.1. Initial & Boundary Conditions

First, the initial and boundary conditions for the cavern case are discussed, followed by the natural cavern case (EPE-S43).

$$\text{Boundary Condition:} = \begin{cases} \sigma_x^{cav} = P_c \cdot sin(\alpha) \cdot l \cdot w & \text{at } -500 < y < 500, -1000 < x < -800 \\ \sigma_y^{cav} = P_c \cdot cos(\alpha) \cdot l \cdot w & \text{at } -500 < y < 500, -1000 < x < -800 \\ u_x = 0 & \text{at } -1000 < y < -1000, x = -1000 \\ u_y = 0 & \text{at } y = -1000, -1000 < x < 1000 \end{cases} \tag{3.11}$$

$$\text{Initial Condition:} = \begin{cases} \sigma_{xx} = \sigma_{yy} = \sigma_{zz} = \sigma_v & \text{at } -1000 < y < 1000, -1000 < x < 1000 \\ u_x = u_y = 0 & \text{at } -1000 < y < 1000, -1000 < x < 1000 \end{cases} \tag{3.12}$$

where P_c is the cavern pressure (discussed in detail in next subsection), α the inclination angle of the cavern, l and w the dimensions of the element and σ_v the confining pressure.
The confining pressure used for the initial condition is calculated at the center of the cavern with the following formula:

$$\sigma_v = \rho_{litho} \cdot g \cdot H \tag{3.13}$$

where ρ_{litho} is the density of the overburden, g the Earth's gravity approximately equal to 10 $\frac{m}{s^2}$ and H the depth in meters. There has been assumed that the density of the overburden is equal to the density of the rock salt.
Similar boundary and initial conditions are used for the natural cavern case, though as the dimensions of the mesh vary (fig. F.3), a different confining pressure is used.

3.3.2. Cavern Pressure

The pressure in the cavern is determined by the amount of hydrogen currently stored, while the outside pressure is represented by the confining pressure. During operation, the pressure in the cavern can change depending on the storage condition (loading or unloading). Caglayan and Weber (2020) mention guidelines to regulate the cavern pressure with a maximum cavern pressure of 75% of lithostatic stress measured at the hanging wall (shallowest point of the cavern). The minimum cavern pressure is equal to 25% of lithostatic pressure measured at the foot wall (the deepest part of the cavern). This means that the resulting pressure is always applied to the inside of the cavern. Since viscoplastic strain is dependent on loading history, the cavern pressure will be increased from zero (equilibrium condition) towards the desired pressure. For the cylindrical cavern case, the cavern pressure will vary with a constant increment between zero and ten MPa, which is in accordance with the guidelines provided by Caglayan and Weber (2020).

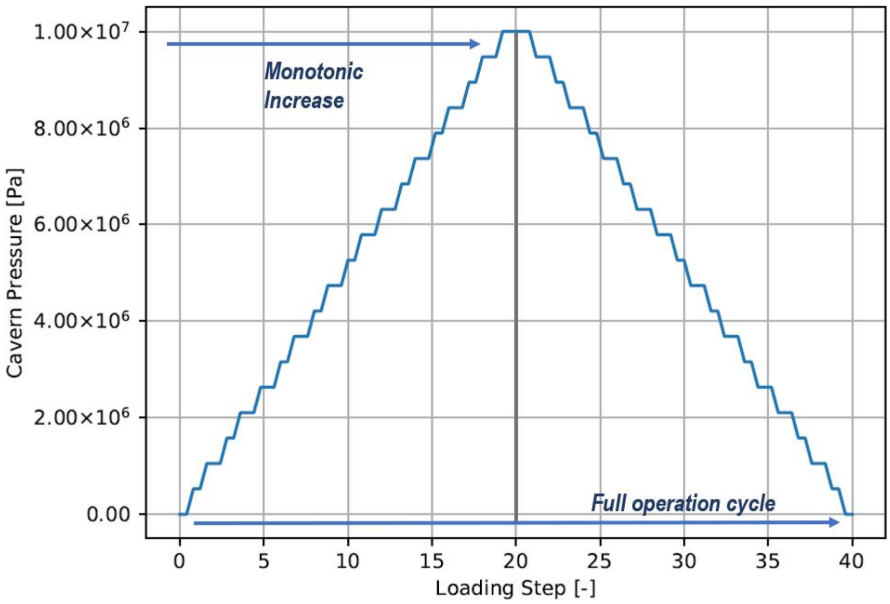

Figure 3.5: Cavern operation cycle: pressure profile of the cavern for one operation cycle of hydrogen injection and extraction.

For the EPE-S43 mesh case, the pressure is defined differently (fig.3.6). The pressure will start again from zero, the equilibrium condition, and will be increased to the minimum required cavern pressure according to Caglayan and Weber (2020). In practice, the cavern pressure does not start from zero as it is first filled with cushion gas (often N_2 gas) which regulates the pressure and prevents the hydrogen from mixing with the cavern sump (bottom of the cavern that contains insolubles of the leaching process). In this thesis, this phase is referred to as the 'initial phase' that mainly stabilizes the pressure in the cavern. The end point of this phase is called the empty cavern state, the cavern contains a small amount of cushion gas and no hydrogen is present. The cavern is then ready for operation and the cavern is loaded and unloaded under the aforementioned pressure conditions.

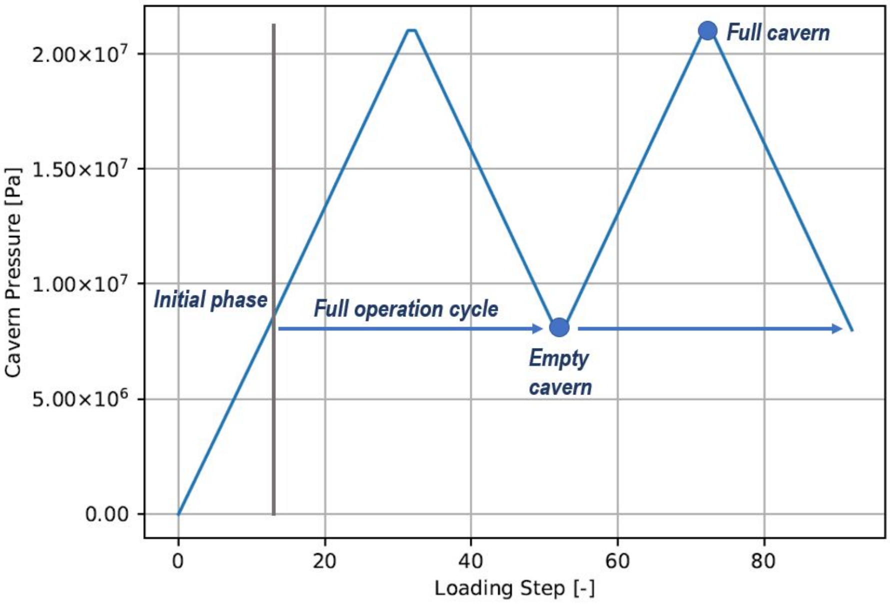

Figure 3.6: Operation regime including initial phase: pressure profile of two injection and withdrawal cycles.

Since an actual cavern is a 3D object and the sonar measurements obtained produce 2D cross-sections at a specific angle, multiple meshes have been created to which the boundary conditions are applied to check how the simulator performs on a 'real' cave (figure I.3). After simulation, a deformed mesh is created to check the volume difference of the cavern. As the working volume of the cavern is known, an estimate of the volume loss due to viscoplastic deformation is obtained from the difference between the original and deformed mesh.

3.3.3. Consistency Analysis Elastic Predictor

A similar procedure for consistency analysis has been performed as in Makhmutov (2020). The validation of the model has been done by comparing the numerical and analytical solution. With a predefined displacement in both directions defined as a function of coordinates such as:

$$u(x,y) = sin\left(\frac{\pi x}{L}\right)sin\left(\frac{\pi y}{W}\right) \tag{3.14}$$

$$v(x,y) = sin\left(\frac{\pi x}{L}\right)sin\left(\frac{\pi y}{W}\right) \tag{3.15}$$

where x and y are the coordinates on the mesh and the length (L) and width (W) equal to 2000m.
With these predefined displacements, strains and stresses and nodal forces can be calculated analytically. The calculated nodal forces are used as input in the numerical simulation that recalculates the displacement, strains and stresses. Then a comparison is made between the two by taking the absolute value of their difference, the absolute error. The absolute error is normalized to obtain the relative error. This procedure is performed a total of four times, each with a mesh refinement that divides the elements of the mesh in half (figures H.1). Then, the order of convergence for the discretization method is determined by the following formula:

$$q \approx \frac{log\left(\frac{e_{\text{new}}}{e_{\text{old}}}\right)}{log\left(\frac{h_{\text{new}}}{h_{\text{old}}}\right)} \tag{3.16}$$

where q is the order of approximation, e_{new} and e_{old} the relative errors compared to each other and h_{new} and h_{old} the step sizes.

3.3.4. Sensitivity Analysis of Elasto-Viscoplastic Model

A parametric study is performed to check the sensitivity of the model. Therefore, key parameters that influence the model response are introduced and the variation of these parameters is tested. For this study a similar cavern pressure range as the cylindrical cavern case is used (fig.3.5). The parameters under investigation are chosen based on differences in key parameter values found according to Khaledi and Mahmoudi (2016a) (Table 3.2) and from laboratory studies Hansen (1978) & Herrmann and Wawersik (1980) which defined a range for some parameters. Table 3.3 lists the input values used for the parameters under investigation.

Table 3.2: Material parameters for elasto-viscoplastic model from different rock salt samples across the world (adapted from Khaledi and Mahmoudi (2016a).

		Sonderhausen mine	Salado mine	Jintan mine	Asse mine
Elastic Parameters	K [MPa]	18,115	18,115	18,115	18,115
	G [MPa]	9842	9842	9842	9842
Viscoplastic Parameters	μ_1 [day^{-1}]	5.06e-7	5.06e-7	5.06e-7	5.06e-7
	N_1	3	3	3	3
	n	3	3	3	3
	a_1 [MPa^{-1}]	0.00005	0.00005	0.00009	0.00004
	η	0.7	0.7	0.7	0.6
	β_1 [MPa^{-1}]	4.8e-3	4.8e-3	4.8e-3	4.8e-3
	β	0.995	0.995	0.995	0.995
	m_v	-0.5	-0.5	-0.5	-0.5
	γ	0.11	0.095	0.095	0.11
	R [MPa]	5.4	5.4	5.4	5.4

Table 3.3: Input values for sensitivity analysis, * indicates base case values.

	Values				
K (GPa)	14.5	16.3	18.1*	19.9	21..7
μ (GPa)	7.8	8.8	9.8*	10.8	11.8
μ_1 (day^{-1})	$5.06 \cdot 10^{-5}$	$5.06 \cdot 10^{-6}$	$5.06 \cdot 10^{-7}*$	$5.06 \cdot 10^{-8}$	$5.06 \cdot 10^{-9}$
n (-)		2.90	3.00*	3.10	
α_1 (MPa^{-1})		$4 \cdot 10^{-5}$	$5 \cdot 10^{-5}*$	$7 \cdot 10^{-5}$	
γ (-)	0.09	0.10	0.11*		

3.4. Source Code

The main goal of this thesis is to build a simulator that captures certain aspects of the mechanical response of rock salt. This simulator is built in Python and the source code is available on GitHub at the following repository (https://github.com/diabolik13/Cavern/tree/vp). This repository contains a 'README' file that contains the main idea, a prerequisite file for the installation of all used packages, a folder with all the different meshes used, and the files with scripts to run the model.

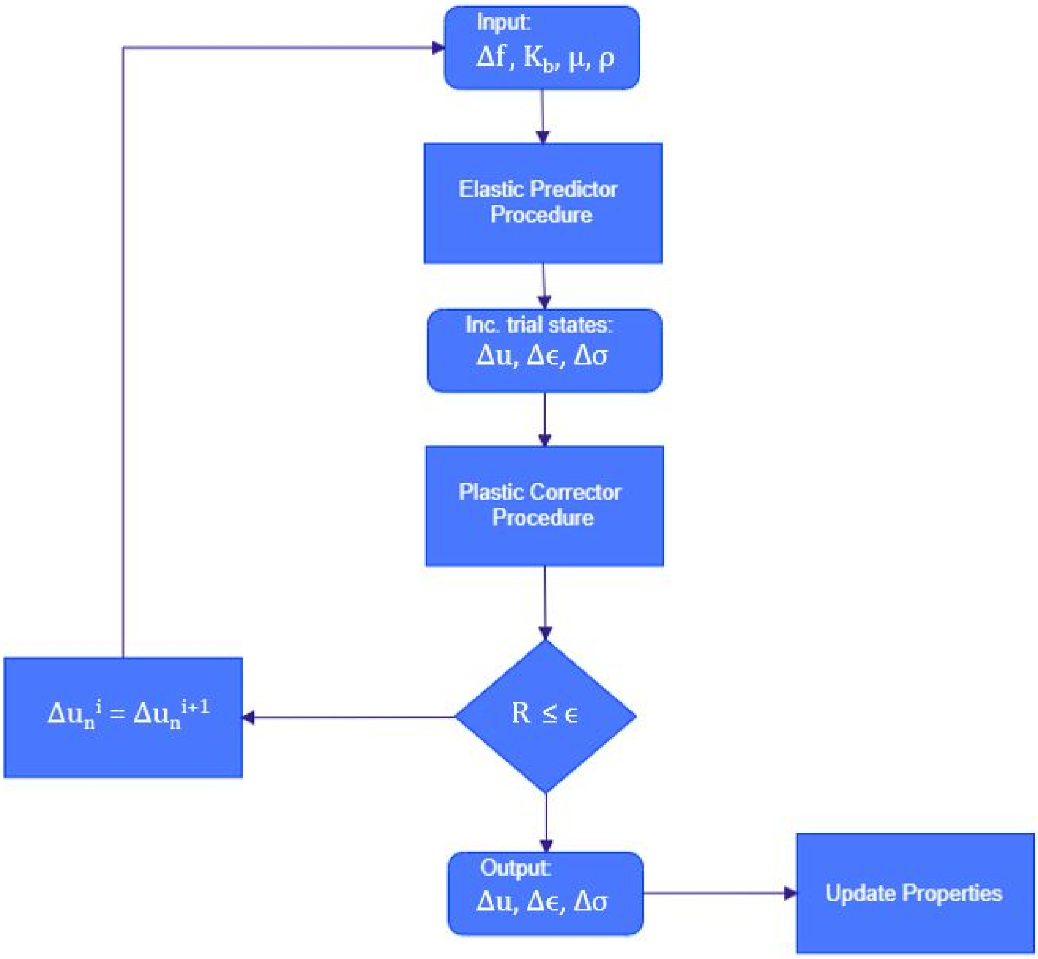

Figure 3.7: Schematic overview of the general procedure of the model including both the elastic predictor and plastic corrector steps.

4 Results

In this chapter the results of the previously described test cases are presented. First, the results for the cylindrical cavern shape for different loading criteria are displayed. For the cylindrical cavern case, a density of 2000 $\frac{kg}{m^3}$ is used for both the overburden and the rock salt material in contrast to the actual rock salt density. Subsequently, the results of the application of the natural cavern mesh (EPE-S43) are shown. Finally, the results for both the consistency and sensitivity analysis are presented.

4.1. Monotonic Cavern Pressure Increase: 0 - 10 MPa

The purpose of this section is to record the response of the system to monotonically increasing cavern pressure. Figure 4.1 displays the displacement, strain and stress in both x-direction and y-direction. Negative displacements are oriented against their corresponding axes, positive displacements are oriented along their corresponding axes. Negative strain corresponds to compression, while positive strain represents extension of the domain. Negative stress imply that stress is exerted into the cavern, while positive stresses indicate stresses that point outwards.

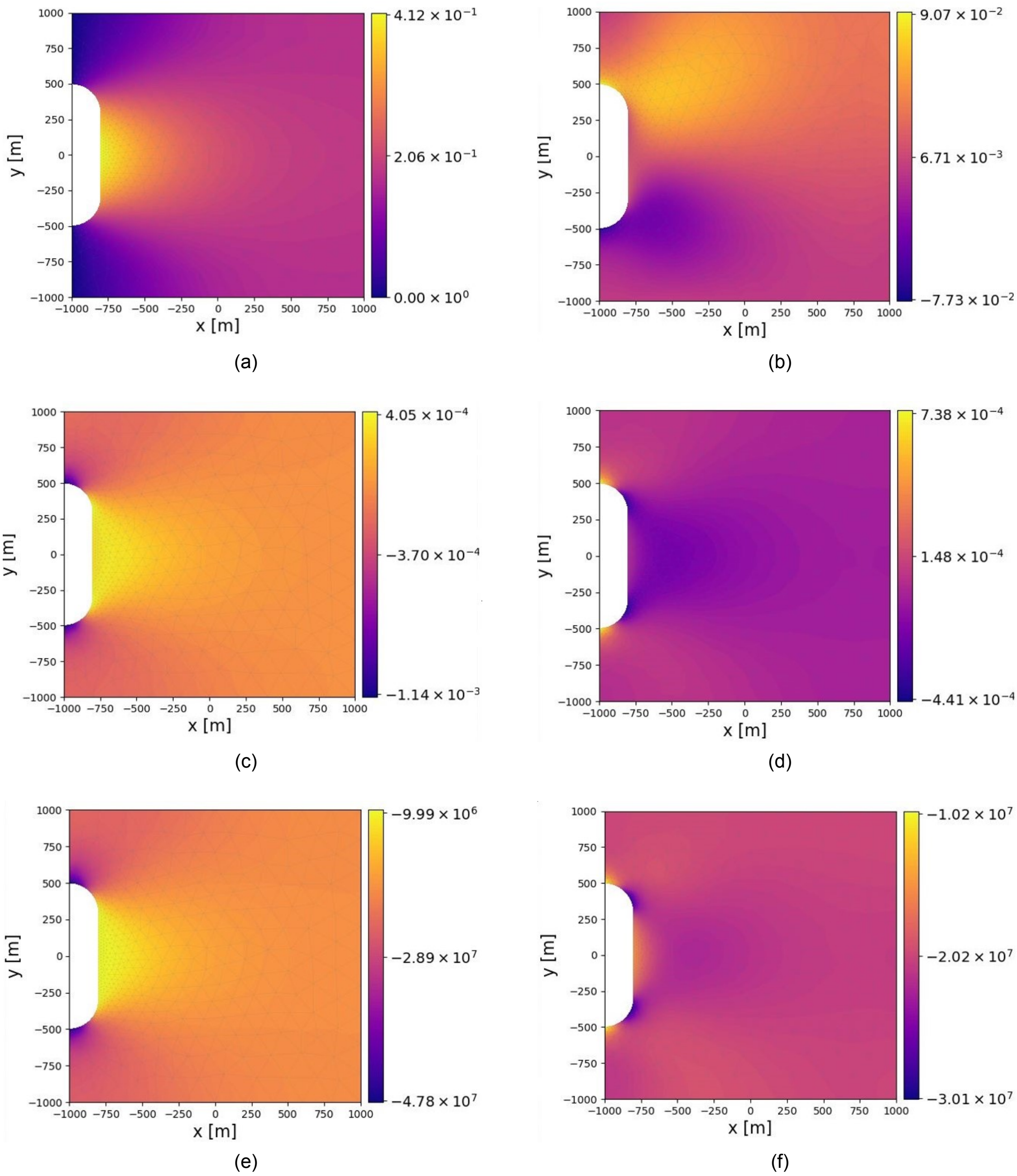

Figure 4.1: Behaviour around the cavern for monotonic increase in pressure at 10 MPa; (a) displacement in x-direction (m); (b) displacement in y-direction (m); (c) strain in x-direction (-); (d) strain in y-direction (-); (e) stress in x-direction (Pa); (f) stress in y-direction (Pa).

The displacement in x-direction (a) is always positive with the greatest displacement being approximately 0.4m visible on the vertical part of the cavern wall. The displacement in y-direction is greatest at the curved part of the cavern (about 0.09m) and shows opposite signs when the cavern pressure pushes on the material. Since the initial conditions state that there is no initial displacement, all the displacements work against the rock salt formation. For strain in x-direction, the vertical cavern wall displays the greatest values (approximately 4E-05) and the curved cavern wall the lowest. This implies that the cavern would squeeze in the curved parts and extend at the vertical cavern wall. Similar reasoning can be applied to the y-direction in which the cavern would extend at the curved parts and contract at the vertical cavern wall. Identical patterns as strain are visible for the stress response in both directions. Since there is an initial stress condition, all the values are negative, meaning the stresses

are directed to the inside of the cavern. For the x-direction, the smallest stresses are visible at the vertical cavern wall. This is due to the cavern pressure exerting most of the stress towards the vertical cavern wall and at a constant initial stress condition results in small stresses. Similar reasoning can be applied for the y-direction, although the magnitude of stress is more negative (magnitude differences of 10 between the smallest value compared to the x-direction). This is mainly because the cavern pressure acts less in this direction, which is also visible in the displacement result. The results confirm that under the applied pressure the cavern shrinks and thus compression is visible.
The following figure, fig.4.2, shows the mesh result for both the first stress invariant and the squared second deviatoric stress invariant.

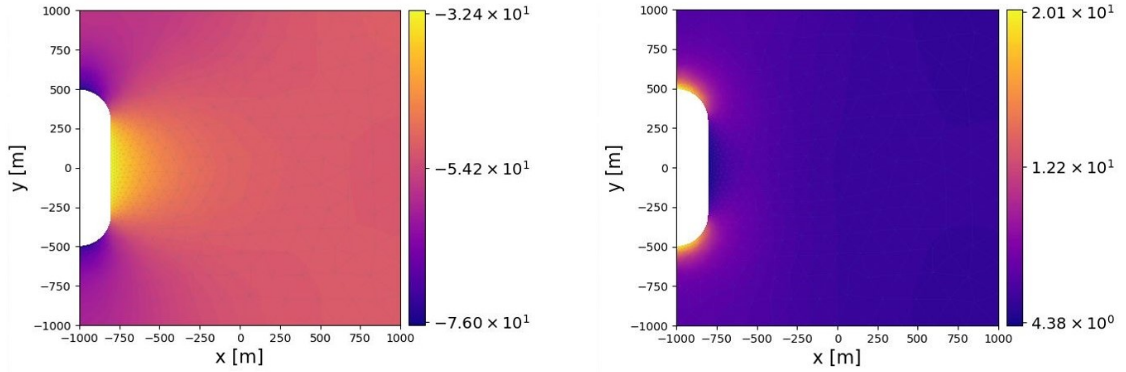

(a) (b)

Figure 4.2: Mesh plot for first stress invariant I_1 (a) and square root of the second deviatoric stress invariant $\sqrt{J_2}$ (b) at 10 MPa cavern pressure.

The first figure (a) displays the first stress invariant showing the most negative values at the corners of the cavern and the smallest negative values at the vertical cavern wall. For the second deviatoric stress invariant (J_2) the largest values are visible at the curved edges of the cavern, while the lowest are found at the vertical cavern wall.
The stress states for point N during the monotonically increasing cavern pressure are displayed in figure 4.3(a). Figure 4.3(b) shows the yield function around the cavern at a cavern pressure of 8 MPa. This cavern pressure is chosen because at this pressure the largest amount of points start to behave viscoplastic.

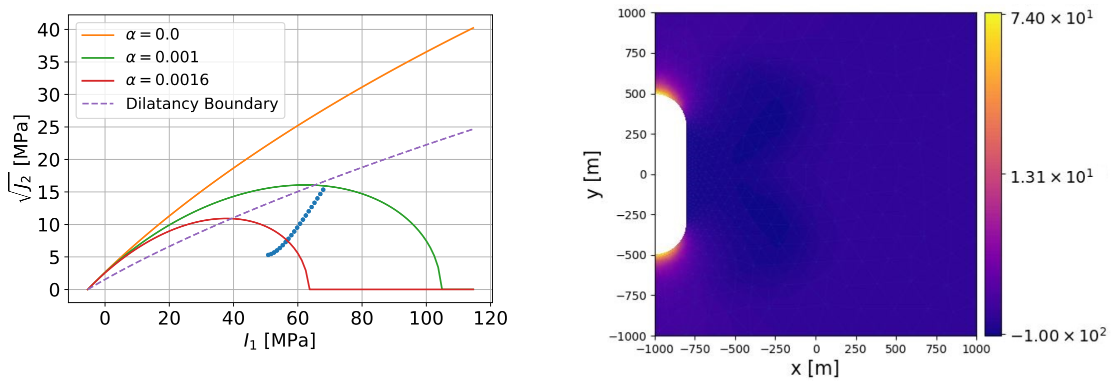

(a) (b)

Figure 4.3: Stress states (blue dots) for monotonic cavern pressure increase from 0 to 10 MPa, with predefined yield surface (red), final yield surface (green) and ultimate failure surface (orange) for $\theta = 49°$ (a) and yield function, F^{vp}, values over entire mesh (b).

Initially, the point is within the predefined yield function (red area), which means that only elastic deformation occurs. After increasing the pressure a number of times, the point is on the yield surface,

causing viscoplastic deformation to occur. This also activates the hardening parameters that rely on viscoplastic strain to increase the size of the yield surface. This process takes place several times until the final cavern pressure is reached and the final yield surface is formed (green). The compressibility-dilatancy boundary (purple) or short dilatancy boundary is also visualized. Khaledi and Mahmoudi (2016b) state that at this boundary the behaviour of rock salt changes from a ductile material response in the compressibility domain (below the boundary) to a brittle material response in the dilatancy domain (above the boundary). In (b) the values for the yield function over the entire mesh are plotted at a cavern pressure of 8 MPa. This pressure was chosen because at this moment most of the viscoplastic deformation is visible. Moreover, this figure shows that viscoplastic behaviour is mainly activated on the curved parts (yellow) of the cavern and that the vertical wall of the cavern is not activated (negative sign of yield function).
The final figure of this section, 4.4, shows the total strain, viscoplastic strain and displacement of point N.

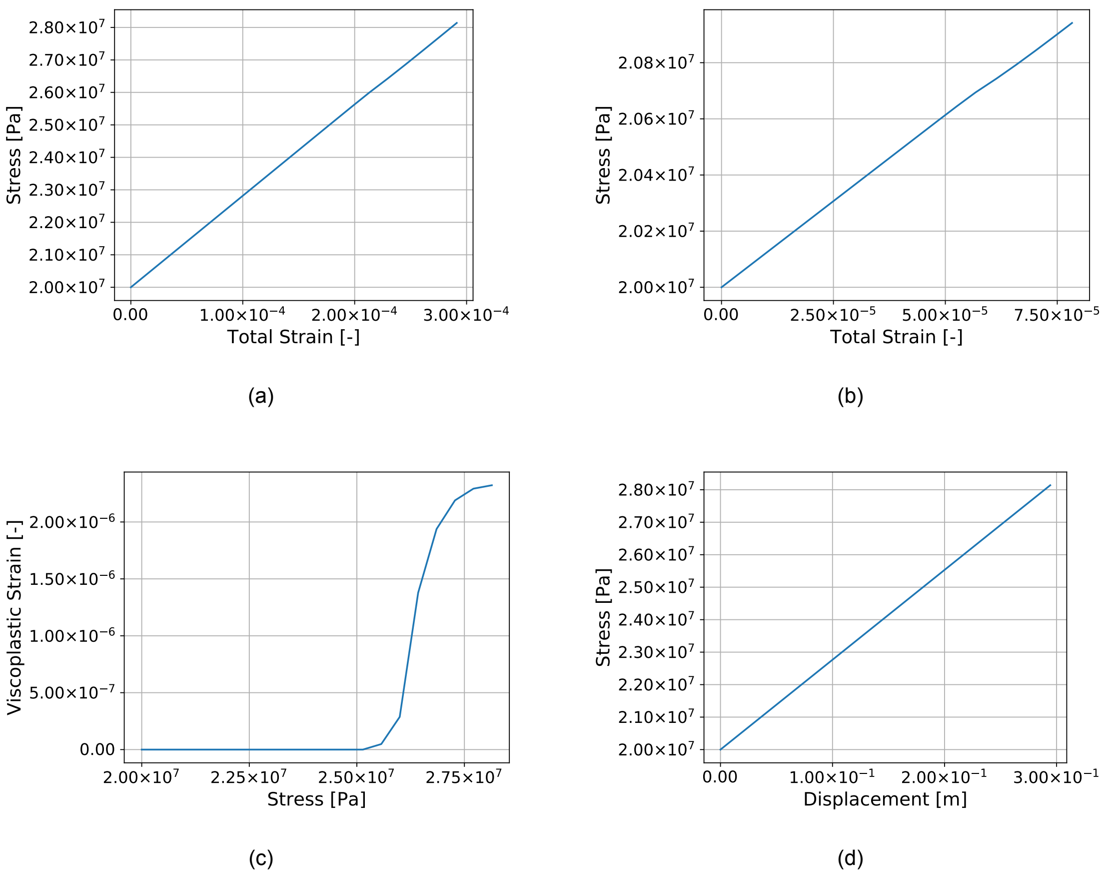

Figure 4.4: Response of point N during monotonically increasing cavern pressure: (a) strain versus stress in x-direction; (b) strain versus stress in y-direction; (c) stress versus viscoplastic strain in x-direction; (d) displacement versus stress in x-direction.

Fig.4.4(a) and 4.4(b) represent the total strain in x and y-directions. From these figures, it is difficult to determine whether viscoplastic strain is occurring as the line appears linear. Therefore, figure (c) shows the viscoplastic strain occurring in the x-direction (y-direction is negligible). As can be seen, viscoplastic strain occurs at higher cavern pressures, but the magnitude of the viscoplastic strain is almost 100 times lower than that of elastic strain and is therefore hardly visible. This also explains that for the displacement in x-direction, figure (d), a similar almost linear trend is visible.

4.2. Cyclic Loading Condition: 0 - 10 - 0 MPa

This section describes for the same case (cylindrical cavern shape) the response to cyclic loading conditions. This implies that the cavern will undergo multiple cycles of loading and unloading (in total three cycles are used). The first figure, fig.4.5, describes the total and viscoplastic strain at two different points (N & T, see fig.3.4).

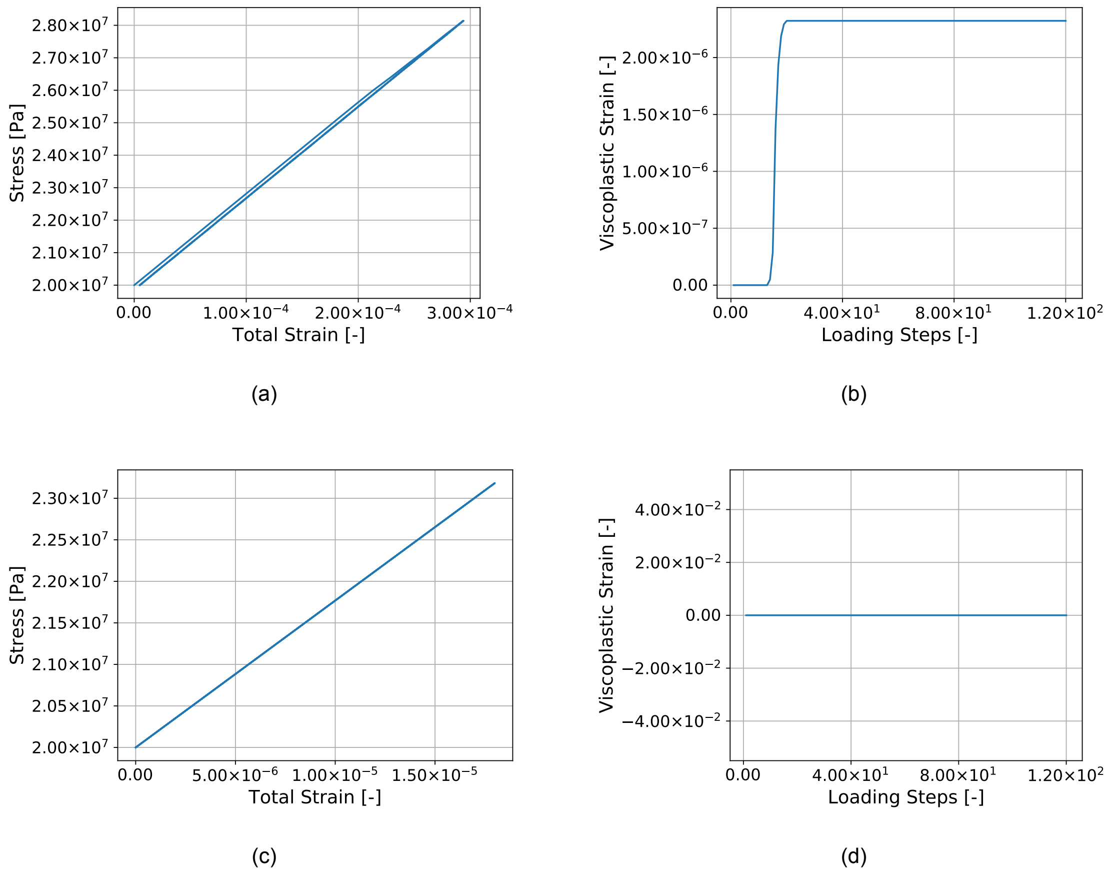

Figure 4.5: Cyclic loading response of point N: (a) strain versus stress in x-direction; (b) loading steps versus viscoplastic strain in x-direction; Cyclic loading response of point T: (c) strain versus stress in x-direction; (d) loading steps versus viscoplastic strain in x-direction.

The material is loaded first (cavern pressure increases) in which the viscoplastic strain contribution is not visible, but after unloading the material the contribution of viscoplastic strain is visible. Since viscoplastic deformation is irreversible, it persists even after unloading the material. Further viscoplastic deformation may occur upon reloading, but this is not visible from figure (b). This can also be explained using the stress state figure (fig.4.3a) in which one could see that if the material is loaded up to the same 10 MPa cavern pressure, it will reside inside the (green) yield surface and thus only elastic strain will occur. For the second point (T), which is near the vertical part of the wall, no viscoplastic strain is visible, which is in accordance with figure fig.4.3b showing negative yield function values on the vertical cavern wall.

The displacement response for the cyclic loading mechanism at point N is displayed in figure 4.6.

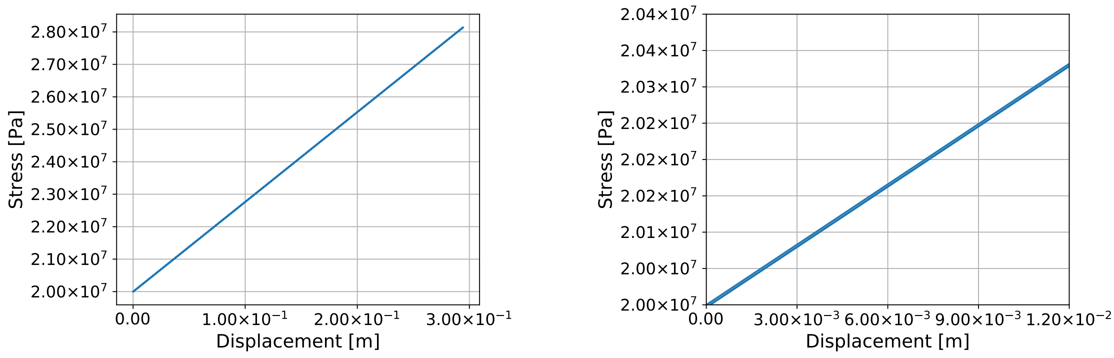

(a) (b)

Figure 4.6: Displacement in x-direction vs stress response for cyclic loading conditions at point N (left; original response, right; zoomed-in response).

Since the contribution of viscoplastic strain is so small compared to the elastic component, almost no change in displacement is visible. Only when zooming in on the figure, a small difference in displacement between the loading and unloading condition is visible, this difference is due to the occurrence of viscoplastic strain.

Both the yield and dilatancy surfaces are functions of Lode's angle. To compare the stress paths of point N and T around the cavern, independent of the Lode's angle, the stress points are displayed for $\theta = 60^\circ$ (fig.4.7). Therefore, the second deviatoric stress invariant (J_2) is scaled using the following equation:

$$\text{scaled } J_2 = J_2 \frac{F^{dil}(I_1, 60^\circ)}{F^{dil}(I_1, \theta)} \tag{4.1}$$

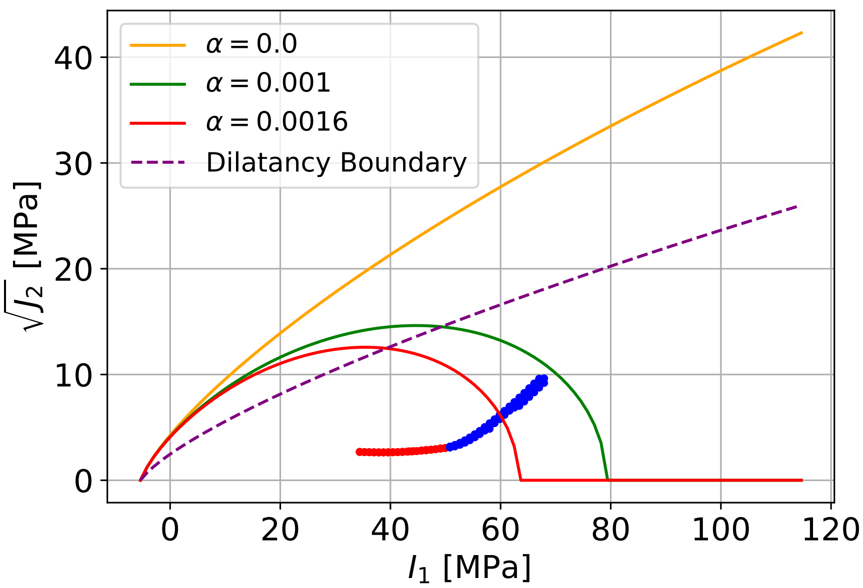

Figure 4.7: Stress states under cyclic loading conditions for point N (blue) and T (red). The red boundary defines the predefined yield surface whereas the green boundary defines the final yield surface, the orange boundary illustrates the ultimate surface while the dilatancy boundary is marked purple.

The blue dots indicate the stress states at point N, while the red dots indicate the stress states at point T. As mentioned earlier for point N, viscoplastic deformation occurs and the yield surface is increasing. Another thing to note is that when reapplying the load (increasing the cavern pressure) the stress states for this point are slightly different. One cause of this may be that the geometry changes slightly and therefore reloading is performed in a different stress path. Point T remains within the initial prescribed yield surface, which means that it is fully elastic.

4.3. Natural Cavern Mesh Application: EPE-S43

The next section is dedicated to the results for the EPE-S43 mesh application. In this section the actual rock salt density described in table 3.1 is used. For the application of the natural cavern mesh, the results for displacement, strain and stress are visualized in figure 4.8. Notations similar to those used for the monotonic cavern pressure results are used.

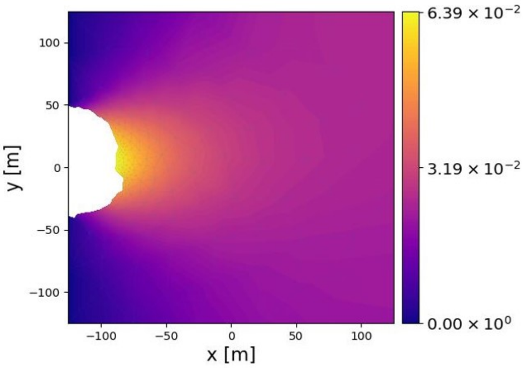

(a)

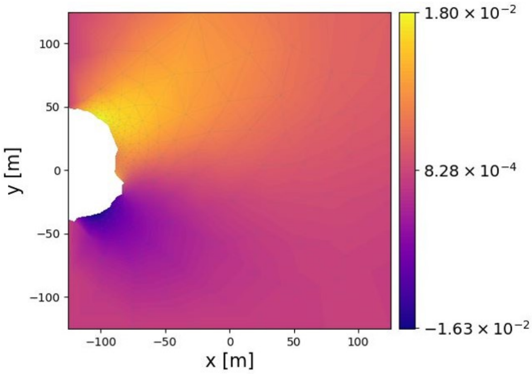

(b)

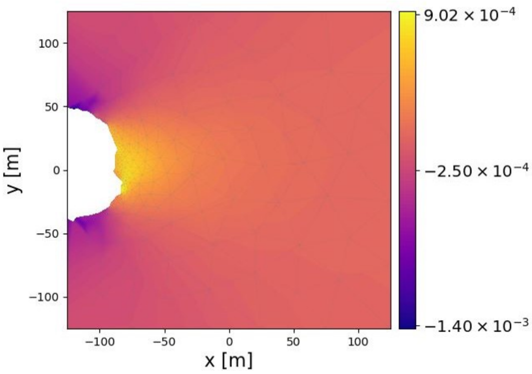

(c)

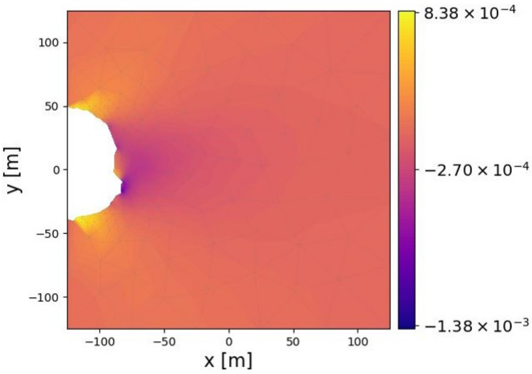

(d)

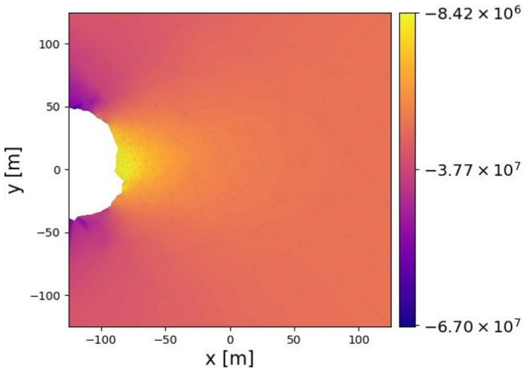

(e)

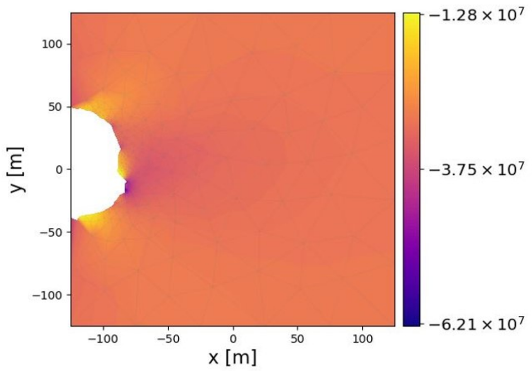

(f)

Figure 4.8: Elasto-viscoplastic response of mesh 67L at 21 MPa for (a) displacement in x-direction (m); (b) displacement in y-direction (m); (c) strain in x-direction; (d) strain in y-direction; (e) stress in x-direction (Pa); (f) stress in y-direction (Pa).

Similar trends are visible as for the cylindrical cavern, meaning that the cavern compresses under the applied pressure. Since the initial stress is different due to the depth difference, the stresses vary with respect to the cylindrical cavern mesh. In addition, the displacement is much smaller compared to the original cylindrical cavern mesh due to differences in dimensions. The natural mesh size ranges from -150 to 150m while the cylindrical cave mesh ranges from -1000 to 1000m. Because the shape of the

natural cavern mesh is more irregular, more curved and vertical parts are seen that follow the same trends as similar parts of the cylindrical cavern mesh.
Figure 4.9 describes the response of the natural mesh to cyclic loading, again three loading cycles are used. Note that a different operation cycle (fig.3.6) is used with respect to the cylindrical cavern case. The total and viscoplastic strain for point O are displayed in figure 4.9.

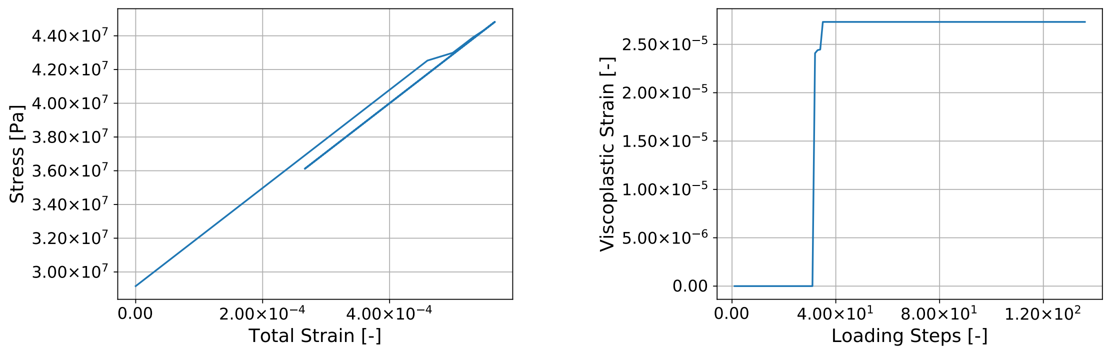

(a) (b)

Figure 4.9: Cyclic loading response of (a) strain vs stress; (b) loading steps vs viscoplastic strain, both in x-direction at point O.

For the total strain component, it increases linearly with stress up to 4.20E7 Pa, after which more deformation occurs. At this point viscoplastic strain grows from zero to 2.5E-5, meaning that the extra deformation most likely occurred due to viscoplasticity. After reaching the maximum cavern pressure, the cavern is unloaded and permanent plastic deformation is still visible. Due to the different applied operation cycle, the cavern is not fully unloaded. The minimum cavern pressure is reached according to the guidelines in which mostly cushion gas is present. Any additional cycles do not produce more viscoplastic strain and the whole response becomes elastically, as shown in figure (b). Comparing the magnitude of viscoplastic strain with that of the cylindrical cavern mesh, it can be noted that the magnitude in the natural cavern mesh is larger. This is mainly due to the fact that viscoplastic strain depends on the stress state. Since that within the natural cavern mesh higher cavern pressures are applied, higher magnitudes of viscoplastic deformation are visible.
Simulation of the real cavern case has been performed to understand how much loss of volume will occur due to viscoplasticity. The total working volume in the cavern is equal to 310,032 m^3 of gas. Table 4.1 gives an overview of the volume loss occurring in the EPE-S43 cavern.

Table 4.1: Volume loss of the cavern due to viscoplastic behaviour

	Volume Loss	
	Percentage (%)	Volume (m^3)
EPE S43	$3.1 \cdot 10^{-4}$	96

From previous results it can be seen that (almost) all viscoplastic deformation occurred during the first loading cycle and that viscoplastic deformation is between 10 and 100 times smaller compared to the total strain. Taking this into account, the small volume loss (96 m^3) is possible. It must be said that this is a rough approximation to estimate the contribution of viscoplastic deformation.

4.4. Consistency Analysis Elastic Predictor

Consistency analysis is performed on the elastic predictor step to determine the accuracy of the unknown quantities. The relative error (the difference between the numeric and analytic solution) for different mesh sizes is displayed in figure 4.10. The rate at which the numerical approximation decreases is represented by the slope of the line (order of accuracy). On a log scale plot, the order of the unknown quantity is found by plotting the error of the unknown quantity against the element size. Thus, the solution for displacement is second-order accurate, while both stress and strain are first order-accurate. For the solution of both the analytical and numerical calculation on the most refined mesh see appendix H.

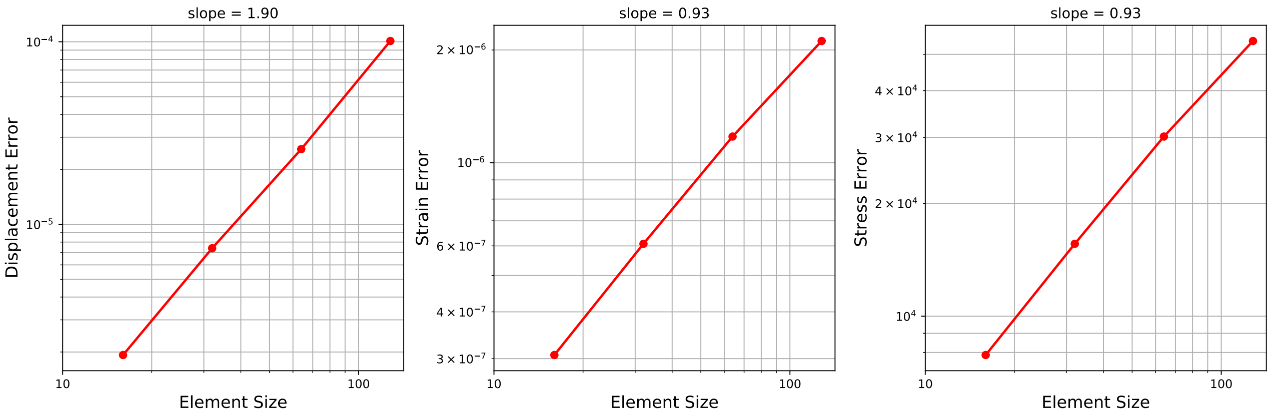

Figure 4.10: Order of accuracy for displacement, strain and stress.

4.5. Sensitivity Analysis of Elasto-Viscoplastic Model

This section shows the effects of six different parameters on the model using the cylindrical cavern mesh. The bulk modulus (K_b) and shear (μ) modulus measure the resistance against deformation due to uniform compression and shearing, respectively. Ten percent incremental differences from the base scenario are used for these two parameters. One of the viscoplastic parameters is the fluidity parameter, μ_1, which is generally the inverse of viscosity. The phase change parameter, n, is related to the onset of dilatancy. Hardening coefficient α_1 controls the size of the viscoplastic yield surface and γ is usually related to the short-term failure boundary of rock salt. All the parameters in the figures are calculated at point N (fig.3.4) in the mesh because viscoplastic deformation occurs at this point.

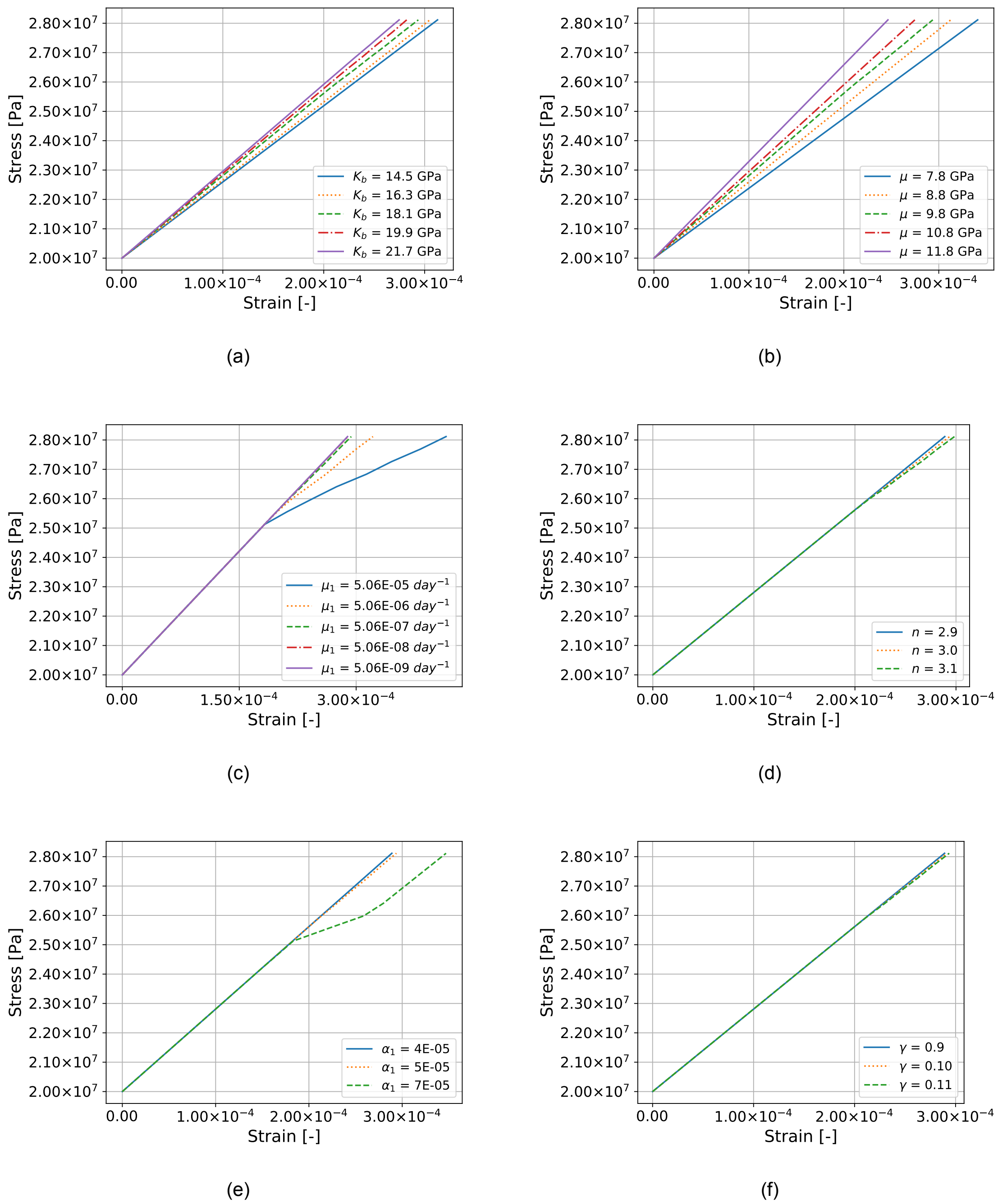

Figure 4.11: Sensitivity analysis for point N on strain in x-direction for (a) bulk modulus; (b) shear modulus; (c) fluidity parameter; (d) phase change coefficient; (e) hardening coefficient; (f) gamma.

The parameters examined were chosen based on differences found in laboratory experiments and the differences in values found from different salt samples. The bulk (K_b) and shear modulus (G or μ) are varied as the material can consist of multiple materials instead of being pure halite (rock salt) and therefore large differences in values have been investigated. Khaledi and Mahmoudi (2016a) stated that the fluidity coefficient, μ_1, the phase change coefficient (n) and γ are the most sensitive viscoplastic parameters. Furthermore, table 3.2 also shows that the hardening coefficient α_1 and γ have different values for different rock salt samples and are therefore included in the parametric study. Then three other parameters N, β and β_1 were examined, but no obvious differences were found.
The biggest differences within figure 4.11 can be seen for the shear modulus, the fluidity parameter and the hardening coefficient (α_1). Comparing the shear modulus differences with the bulk modulus results, rock salt is more sensitive to shearing than to uniform compression. When the fluidity parameter is increased to, for example, $5.06 \cdot 10^{-5}$, the strain at the highest pressure is about 1.5 times that. Higher fluidity values result in lower viscosity and more deformation is observed. This is in accordance with the findings of Khaledi (2017). A Higher value for the hardening coefficient α_1 results in more deformation, as the overall hardening coefficient α will increase, increasing the magnitude of the yield function and thus the amount of viscoplastic deformation occurring. The sensitivity of the model to other viscoplastic parameters such as the phase change coefficient (n) and γ are only small where it is most sensitive to an increase in the phase change coefficient.

5 Discussion & Conclusion

The project aimed to develop a simulator that records the mechanical response of rock salt under stress variation. In detail, most attention has been focused on the rate-dependent process called viscoplasticity. This section discusses the limitations and summarizes the key findings of the project.

5.1. Discussion

Some points and presumptions should be mentioned for the current state of the simulator. First, the initial stress condition needs to be clarified. In this study, it was decided that the initial stress is calculated at a single point in the mesh and constant over the entire mesh. This was done to make the results easier to understand. An example of this is the stress on the vertical part of the cylindrical cavern wall for monotonically increasing cavern pressures. If the initial stress condition were dependent on the depth at that specific location, one would see an increase in stress as going deeper into the subsurface. In addition, the overburden density is equal to the density of rock salt, in reality this is not true. To account for a difference in overburden density, one could add an extra force on top of the mesh moving downwards to simulate density differences. In addition, the first yield surface is predefined, as the initial value of the hardening parameters is set manually. In the first iteration (initial stresses only, no cavern pressure) it was taken into account that the hardening parameters ensure that the system response is fully elastic and thus no viscoplastic deformation occurs at this step. Since the hardening parameters are set to the same value for each point, the development of viscoplastic strain may not be accurately predicted at some points. Another assumption is made for the derivative of the residual function where the derivative of viscoplastic strain with respect to displacement is neglected due to complexity. Addition of this term would mean that the simulator converges more quickly to the exact solution, although no convergence problems were encountered without this term. With regards to the volume loss calculation on the natural mesh, it has been assumed that with only eight different meshes the loss of the entire cavern can be described. In reality, this is not the case and 3D simulations must be used to accurately determine the amount of volume, although this calculation is mainly used as a very rough approximation to recognize the impact of viscoplastic deformation on the cavern volume. A thorough parametric study is recommended to understand how each viscoplastic parameter behaves under different loading conditions. A small sensitivity analysis has currently been performed to specify which parameters affect the model the most.

5.1.1. Review Assumptions and Limitations

Assumptions made in the development of the model place limitations on the accuracy of the results. This section discusses the effects of the assumptions and their limitations for the current model.

2D Plane strain: This assumption is mainly proposed for simplicity of the model. The assumption can be relaxed when switching to 3D, which shows the nature of the problem.
Isotropic and homogeneous material: Currently, the model has only been tested for isotropic and homogeneous material conditions. To apply anisotropic conditions to the elastic model, the notation for stress and strain and thus displacement must be revised (size of matrices and vector change accord-

ingly). The viscoplastic addition does not require much change as it is a stress-dependent model, the terms used to calculate the stress invariants must be revised to capture this behaviour. To apply heterogeneous material properties to the model, different inputs for the elastic moduli must be assigned. However, with regards to the dimensions of the cavern, the details of these different layers must be taken into account. When thin layers of mud of 0.5m are applied against a cavern wall of 200m, the impact of the thin film may not be registered.
Adiabatic conditions (no heat transfer): Because the cavern operates cyclically and the amount of stored hydrogen can fluctuate rapidly, heat transfer must be taken into account. This can be done in two ways, either by modifying the current formulation by adding a component within the elastic and viscoplastic strain definition responsible for temperature fluctuations or by further decomposing the total strain with a 'thermal' strain component.
Equilibrium condition at the start of operation cavern: It is currently assumed that the cavern has already been excavated and that no deformation occurred during the excavation period. It would be more realistic to account for the deformation that occurred during the leaching process by introducing a term for initial strains.
Ignorance of permeability changes, diffusion and chemical reactions in the cavern: Currently, the effects of permeability changes are ignored. During use, it is very likely that changes in permeability around the cavern wall will occur and that leakage may occur. The risk of leakage should be investigated to improve the safety assessment for hydrogen storage and to confirm the usability of the cavern. It has also been assumed that the cushion gas will prevent the hydrogen from reacting with the sump of the cavern, in reality, it could be that a small portion of hydrogen would indeed react with the sump.
No damage evolution or healing effects: Creep effects (time-dependent) have not been taken into account and therefore the evolution of damage has not been recorded. In short, damage evolution occurs when rock dilation begins to occur. To allow for both creep effects and damage development, the creep strain rate can be introduced. Makhmutov (2020) conducted an extensive study of creep deformation and the associated damage evolution. In addition, rock salt tends to heal (repair) some of this damage, although there is currently no reliable model to predict this healing process.
Constant material parameters during simulation: Material parameters can change during simulation due to the operation regime. However, there are still open questions about the modification of the viscoplastic parameters for rock salt.

5.2. Conclusion

The aim was to predict the behaviour of rock salt under different pressure conditions. The results show that the simulator used can capture both the linear elastic response and the nonlinear viscoplastic response. In general, the salt cavern will be compressed (shrinked) by the forces applied. For monotonically increasing cavern pressure, the amount of viscoplastic strain is difficult to estimate due to its small magnitude. It is striking that after a full loading cycle the strain does not return to its original state, which means that irreversible permanent deformation due to viscoplasticity occurs. Over multiple loading cycles, the amount of viscoplastic strain hardly increases as the size of the yield function increases due to the hardening parameters and so the response of the system becomes fully elastic. The yield point originates from the yield surface that determines the onset of viscoplasticity. The simulator can determine this point for each point in the mesh. Based on sonar data, 2D sections of cavern EPE-S43 are created and used as input to the simulator. Similar trends in displacement, strain and stress were noticeable, although with a smaller magnitude due to differences in geometry of the mesh. In addition, the loss of work volume due to viscoplasticity was found to be approximately $3.1 \cdot 10^{-4}$% or 96 m^3. This indicates that viscoplastic deformation on itself does not pose a significant risk to the cyclic storage of hydrogen in salt caverns. A parametric study has been performed showing that the shear modulus μ, hardening parameter α_1 and the fluidity parameter μ_1 have the greatest effect on the sensitivity of the system.
In summary, the elasto-viscoplastic model can be used for many different cases and can predict the elastic and viscoplastic response of the system for different stress conditions. Viscoplasticity can be thought of as a process that takes place after a certain level of stress has been reached and does not increase significantly in magnitude after more operation cycles have been performed. During opera-

tion, viscoplastic deformation itself will not pose significant risks to the stability and serviceability of the cavern.

5.3. Recommendations

Further improvements to the study are here briefly elaborated. Since there is still a lot of room for improvement, this section is mainly devoted to my personal opinion on where possible improvements can be made.

Conversion 2D FEM to 3D FEM: The current 2D simulator can be converted to a 3D. Since salt caverns in nature are three-dimensional objects, this conversion is crucial to talk about the behaviour and draw conclusions from the work performed.
Initial Deformation due to Leaching Process: To optimize the potential for hydrogen storage in salt caverns, some additional caverns must be constructed. When creating such a cavern, the stress and strain state in the subsurface will be disturbed, as a result, initial deformation occurs which must be recorded in the model.
Thermal Effects and Creep Behaviour: To fully understand the macroscopic material response of rock salt for hydrogen storage, two additional components should be added to account for thermal effects (thermal strains) and the time-dependent process (creep deformation).
Impurity of Hydrogen: The main purpose was to describe the stress and strain state of the cavern, although the stored material should also be investigated. Does hydrogen react in the cave, if so, what chemical reactions take place? In addition, the diffusion of hydrogen can also be taken into account.
Permeability Variations and Leakage: Does the permeability change in combination with impurities occur as a result of the operation regime of the cavern? If the permeability changes at specific points in the cavern, is there a risk of leakage and is this measurable? These are questions to be asked and investigated in order to estimate the effects, not only on the stability of the cavern but also for environmental and safety issues.
Laboratory Experiments and Upscaled Test Cases: At present, no real comparison with literature is possible to determine the correctness of the proposed method. This is because creep and viscoplasticity are intertwined. When both factors are taken into account, laboratory experiments such as triaxial tests can quantify the accuracy of the model's prediction. In addition, if data could be provided to the simulator from an actual salt cavern, a comparison can be made between the actual and predicted deformation. Sonar data can be used to identify the actual deformation, which can then be compared to the simulator's predicted deformation over a similar period.
In-Depth Parametric Study: A small sensitivity analysis was performed to identify the most sensitive parameters for the model. To understand the full behaviour of the model and the viscoplastic parameters, an in-depth study of these parameters can provide some useful insights, especially when combined with some laboratory experiments.
Optimisation Current Simulator: The current state of the simulator is not perfect and therefore some adjustments could be made to optimize the use and functionality of the simulator. For example, the computation time could be shortened by using the analytic derivatives or adaptive meshing could be used to identify important locations. Currently, a static mesh is used that does not deform when a load is applied. Therefore, dynamic meshing can be used to show the effects of deformation on the region of interest.

5.4. Significance results & energy transition

This section is mainly devoted to my personal view of the meaning behind the results and the impact that hydrogen storage can have on the energy transition.

5.4.1. Significance of the results

Based on the results, it is feasible to say that additional deformation that occurs as a result of viscoplasticity is only slight (in some cases even negligible) compared to elastic deformation. The question now remains how this research can be used usefully to determine the feasibility of hydrogen storage in salt caverns. First, I would say that understanding the yield criterion of rock salt provides insight into how the material behaves under certain loading conditions. For example, the knowledge of this study can be used to more accurately determine the time-dependent creep behavior, since the yield surface can be divided into two different domains via the compressibility-dilatancy boundary which are dominated by different processes. Second, after comparing this study with that of Makhmutov (2020), it can be concluded that nonlinear deformation occurring during hydrogen storage is mainly due to the time dependent process instead of the stress dependent process (neglecting any temperature effects).

5.4.2. Impact on the energy transition

I think that the impact of hydrogen storage in salt caverns on the energy transition is in itself quite small due to the relatively small amount of energy that can be stored. The technique is mainly used to absorb peaks in energy demand. However, underground hydrogen storage in general could play an important role, especially when including other subsurface storage spaces such as aquifers and depleted gas reservoirs, which contain more storage capacity. For these two storage spaces, there are still many challenges, such as preserving the purity of hydrogen and keeping the hydrogen in place. I think energy storage will play an important role in the future and that for any amount of time or energy necessity there will be specific storage types that are most suitable. For example, for short term storage (low capacity), lithium-ion batteries and flow batteries are becoming increasingly viable. In addition, this suitability is also coupled to environmental factors. For example, competition for subsurface space can become an obstacle. Other uses of the subsurface can include geothermal applications, groundwater abstraction or the mining of materials. It would be fascinating to see how all these applications integrate together.

A Formulation of Finite Element Equations

This section is mainly based on the book of Rao (2005). Using the principle of minimum potential energy, the finite element equations can be derived. The whole procedure is worked out step by step, including the addition of viscoplasticity to the system.

First, the body must be divided into a number of different elements. Second, the displacement model within an element "e" is assumed as:

$$U = \begin{Bmatrix} u(x,y) \\ v(x,y) \end{Bmatrix} = N\vec{Q}^e \tag{A.1}$$

in which $\vec{Q}^e$ is the vector of nodal displacement degrees of freedom of the element (equal to two (x & y)), and N is the matrix of shape functions. The shape functions used for a given triangle are:

$$N1(x,y) = \frac{1}{2A}[(x_2y_3 - x_3y_2) + (y_2 - y_3)x + (x_3 - x_2)y] \tag{A.2}$$

$$N2(x,y) = \frac{1}{2A}[(x_3y_1 - x_1y_3) + (y_3 - y_1)x + (x_1 - x_3)y] \tag{A.3}$$

$$N3(x,y) = \frac{1}{2A}[(x_1y_2 - x_2y_1) + (y_1 - y_2)x + (x_2 - x_1)y] \tag{A.4}$$

where 'A' is the area of the triangle (A = $\frac{1}{2}$ × base × height).

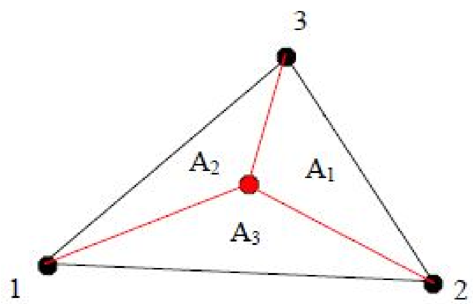

Figure A.1: Example of a triangular element (Rao, 2005)

The element characteristic (stiffness) matrices and characteristic (load) vectors must be derived from the principle of minimum potential energy. For this the potential energy function of the body π_p is written as:

$$\pi_p = \sum_{e=1}^{E} \pi_p^{(e)} \tag{A.5}$$

where $\pi_p^{(e)}$ is the potential energy of the element e given by:

$$\pi_p(u,v) = \frac{1}{2}\int\int_{A^e} \vec{\varepsilon}^T D(\vec{\varepsilon} - \overrightarrow{\varepsilon^{vp}})t dA - \int\int_{A^e} \vec{\phi}^T \vec{U} t \cdot dA - \int_{S_1} \vec{\Phi}^T \vec{U} \cdot dS_1^e \tag{A.6}$$

where A^e is the area of the element, $\vec{\varepsilon}$ the strain, t the thickness of the element, S_1^e is the part of the area of the element over which distributed surface forces act, Φ are the surface forces, ϕ is the vector of body forces per area and $\vec{U}$ is the vector of displacements.
The strain vector $\vec{\varepsilon}$ can be expressed in terms of the nodal displacement vector $\vec{Q}^{(e)}$:

$$\varepsilon = \begin{bmatrix} \varepsilon_{xx} \\ \varepsilon_{yy} \\ \varepsilon_{xy} \end{bmatrix} = \begin{bmatrix} \frac{\partial u}{\partial x} \\ \frac{\partial v}{\partial y} \\ \frac{\partial u}{\partial y} + \frac{\partial v}{\partial x} \end{bmatrix} = \begin{bmatrix} \frac{\partial}{\partial x} & 0 & \frac{\partial}{\partial x} & 0 & \frac{\partial}{\partial x} & 0 \\ 0 & \frac{\partial}{\partial y} & 0 & \frac{\partial}{\partial y} & 0 & \frac{\partial}{\partial y} \\ \frac{\partial}{\partial y} & \frac{\partial}{\partial x} & \frac{\partial}{\partial y} & \frac{\partial}{\partial x} & \frac{\partial}{\partial y} & \frac{\partial}{\partial x} \end{bmatrix} \begin{bmatrix} u \\ v \end{bmatrix} = B\vec{Q}^e \tag{A.7}$$

where [B] is:

$$B = \begin{bmatrix} \frac{\partial N1}{\partial x} & 0 & \frac{\partial N2}{\partial x} & 0 & \frac{\partial N3}{\partial x} & 0 \\ 0 & \frac{\partial N1}{\partial y} & 0 & \frac{\partial N2}{\partial y} & 0 & \frac{\partial N3}{\partial y} \\ \frac{\partial N1}{\partial y} & \frac{\partial N1}{\partial x} & \frac{\partial N2}{\partial y} & \frac{\partial N2}{\partial x} & \frac{\partial N3}{\partial y} & \frac{\partial N3}{\partial x} \end{bmatrix} \tag{A.8}$$

The stresses $\vec{\sigma}$ can be obtained from strains $\vec{\varepsilon}$ as follows:

$$\vec{\sigma} = D(\vec{\varepsilon} - \overrightarrow{\varepsilon^{vp}}) = DB\vec{Q}^e - D\overrightarrow{\varepsilon^{vp}} \tag{A.9}$$

Substitution of equation A.7, A.9 into eq.A.6 yields the potential energy of the elements as:

$$\pi_p^e = \frac{1}{2}\int\int_{A^e} \vec{Q}_{(e)}^T B^T D B \vec{Q}^e dA - \int\int_{A^e} \vec{Q}_{(e)}^T B^T D \overrightarrow{\varepsilon^{vp}} dA - \int_{S_1^e} \vec{Q}_{(e)}^T N^T \vec{\Phi} dS_1 - \int\int_{A^e} \vec{Q}_{(e)}^T N^T \vec{\phi} dA \tag{A.10}$$

Only body and surface forces are considered in this equation. In general, however, some external concentrated forces will also act on some nodes. If $\vec{F_c}$ indicates the vector of nodal forces (acting in the directions of nodal displacement vector $\vec{Q}$ of the total structure or body), the potential energy of the structure can be expressed as:

$$\pi_p = \sum_{e=1}^{E} \pi_p^{(e)} - \overrightarrow{Q^T}\vec{F_c} \tag{A.11}$$

where $\vec{Q} = \begin{bmatrix} Q_1 \\ Q_2 \\ Q_N \end{bmatrix}$ is the vector of nodal displacements of the whole structure or body and N is the total number of nodal displacements or degrees of freedom.
When calculating the potential energy for the whole structure of the body, one can use the sum of overlapping terms:

$$\pi_p = \frac{1}{2}\vec{Q}^T \left[\sum_{e=1}^{E} \int\int_{A^e} B^T D B t dA\right] \vec{Q} - \vec{Q}^T \sum_{e=1}^{E} \left[\int\int_{A^e} B^T D \overrightarrow{\varepsilon^{vp}} dA + \int_{S_1^{(e)}} N^T \vec{\Phi} dS_1 + \int\int_{A^e} N^T \vec{\phi} t dA\right] - \overrightarrow{Q^T}\vec{F_c} \tag{A.12}$$

The static equilibrium configuration of the structure can be found by solving the following necessary conditions (for the minimization of potential energy):

$$\frac{\partial \pi_p}{\partial \vec{Q}} = \vec{0} \text{ or } \frac{\partial \pi_p}{\partial Q_1} = \frac{\partial \pi_p}{\partial Q_2} = \ldots = \frac{\partial \pi_p}{\partial Q_N} = 0 \tag{A.13}$$

With the help of equation A.13, eq.A.12 can be expressed as:

$$\left(\sum_{e=1}^{E}\int\int_{A^e} B^T DBtdA\right)\vec{Q} = \vec{F_c} + \sum_{e=1}^{E}\left(\int\int_{A^e} B^T D\overrightarrow{\varepsilon^{vp}}tdA \int_{S_1^e} N^T\vec{\Phi}dS_1 + \int\int_{A^e} N^T\vec{\phi}tdA\right) \tag{A.14}$$

That is,

$$\left(\sum_{e=1}^{E} K^e\right)\vec{Q} = \vec{F_c} + \sum_{e=1}^{E}\left(\overrightarrow{F_i^e} + \overrightarrow{F_s^e} + \overrightarrow{F_b^e}\right) = \vec{F} \tag{A.15}$$

where

$$K^e = \int\int_{A^e} B^T DBtdA = \text{element stiffness matrix} \tag{A.16}$$

$$\overrightarrow{F_i^e} = \int\int_{A^e} B^T D\overrightarrow{\varepsilon^{vp}}tdA = \text{element load vector due to viscoplastic strain} \tag{A.17}$$

$$\overrightarrow{F_s^e} = \int_{S_1^e} N^T\vec{\Phi}dS_1 = \text{element load vector due to surface forces} \tag{A.18}$$

$$\overrightarrow{F_b^e} = \int\int_{A^e} N^T\vec{\phi}tdA = \text{element load vector due to body forces} \tag{A.19}$$

Part of the contribution to the load vector $\vec{F}$ can be zero for a given problem. In particular, the contribution of surface forces will be not zero for those element boundaries that are also part of the boundary of the structure or body subjected to externally applied distributed load.
The desired equilibrium equations of the total structure or body can now be expressed as:

$$K\vec{Q} = \vec{F} \tag{A.20}$$

where:

$$K = \sum_{e=1}^{E} K^e = \text{assembled (global) stiffness matrix} \tag{A.21}$$

and

$$\vec{F} = \vec{F_c} + \sum_{e=1}^{E}\overrightarrow{F_i^e} + \sum_{e=1}^{E}\overrightarrow{F_s^e} + \sum_{e=1}^{E}\overrightarrow{F_b^e} = \text{assembled (global) nodal load vector} \tag{A.22}$$

B

The Basics of the Yield and Potential Function

A yield function is based upon failure theory. Thus the question arises: how can we predict (static) failure? With ductile materials, failure occurs at the onset of plastic deformation. Given a uniaxial tensile test, failure can be predicted quite easily. In nature, however, this is much more complicated and we do not have one universally applicable method to determine material failure. Instead, we must predict failure by selecting the most appropriate from a range of failure theories. Commonly used failure theories include Von Mises, Drucker-Prager and Tresca failure theory. Each of these theories work reasonably well under certain circumstances based on experimental data.

From failure theory, a yield function is derived by some mathematical procedures. Such a function is a function of stress state and optionally of strain or other parameters. Derived from the yield function, a yield surface (or contour) of stresses is created that defines the onset of plasticity (fig. B.1).

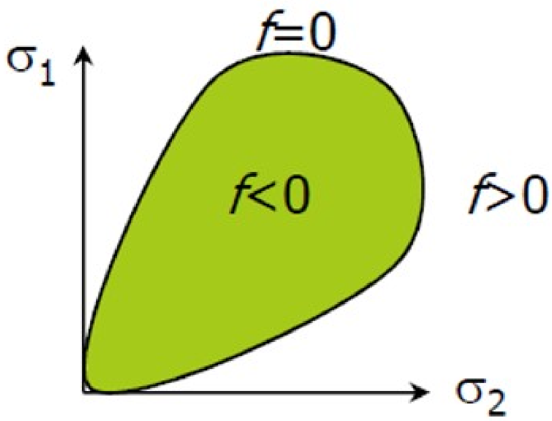

Figure B.1: Yield surface for a given stress state (Brinkgeve, 2019).

Usually the yield surface is convex shaped and the stress state within the yield surface is elastic. For the stress states at the boundaries of the yield surface are said to have reached the yield point and the material starts to behave plastically. Further deformation of the material causes the stress state to remain on the yield surface, even though the shape and the size of the surface may change as the plastic deformation evolves.

In summary, when the stress state is inside the yield surface, the material behaves elastically ($f < 0$). The onset of plastic deformation occurs at the boundaries of the yield surface ($f = 0$). A stress state outside the yield surface is impossible ($f > 0$).

A potential function gives the direction of plastic flow (the rate of plastic deformation). The formulation of the potential function can be exactly the same as the yield function, often referred to as the normality rule (or associated flow rule). The potential function can also differ depending on material properties, in this case it is called a non associated flow rule.
The proposed yield and potential function by Desai and Zhang (1987) are functions of stress invariants and hardening parameters ($f(I_1, J_2, J_3, \alpha, \alpha_q)$). These hardening parameters will change the yield surface for different loading conditions.

C

Stress Invariants

This chapter discusses the definition of stress invariants, how they are calculated and their importance.

Each stress tensor (σ_{ij}) can be expressed as the sum of two other stress tensors, namely the mean hydrostatic stress tensor ($\pi\delta_{ij}$), which tends to change the volume of the stressed body and the deviatoric stress tensor, s_{ij}, which tend to distort the body. In formula this can be written down as:

$$\sigma_{ij} = s_{ij} + \pi\delta_{ij} \tag{C.1}$$

where π is the mean stress given by:

$$\pi = \frac{\sigma_{kk}}{3} = \frac{\sigma_{11} + \sigma_{22} + \sigma_{33}}{3} \tag{C.2}$$

Both tensors have their own respective stress invariants. Technically, the stress invariants associated with the deviatoric stress tensor are called deviatoric stress invariants. But in general, all invariants together are usually called stress invariants.
In tensor notation, the stress tensor and its deviatoric component are described as:

$$\sigma_{ij} = \begin{bmatrix} \sigma_{11} & \sigma_{12} & \sigma_{13} \\ \sigma_{21} & \sigma_{22} & \sigma_{23} \\ \sigma_{31} & \sigma_{32} & \sigma_{33} \end{bmatrix}, s_{ij} = \begin{bmatrix} \sigma_{11} - \pi & \sigma_{12} & \sigma_{13} \\ \sigma_{21} & \sigma_{22} - \pi & \sigma_{23} \\ \sigma_{31} & \sigma_{32} & \sigma_{33} - \pi \end{bmatrix} \tag{C.3}$$

Assuming symmetry of the tensor ($\sigma_{12} = \sigma_{21}$, etc.), the stress invariants are calculated as follows:

$$I_1 = \sigma_{11} + \sigma_{22} + \sigma_{33} \tag{C.4}$$

$$I_2 = \sigma_{11}\sigma_{22} + \sigma_{22}\sigma_{33} + \sigma_{11}\sigma_{33} - \sigma_{12}^2 - \sigma_{23}^2 - \sigma_{31}^2 \tag{C.5}$$

$$I_3 = \sigma_{11}\sigma_{22}\sigma_{33} + 2\sigma_{12}\sigma_{23}\sigma_{31} - \sigma_{12}^2\sigma_{33} - \sigma_{23}^2\sigma_{11} - \sigma_{31}^2\sigma_{22} \tag{C.6}$$

The deviatoric stress invariants are defined as follows:

$$J_1 = 0 \tag{C.7}$$

$$J_2 = \frac{1}{3}I_1^2 - I_2 = \frac{1}{6}\left[(\sigma_{11} - \sigma_{22})^2 + (\sigma_{22} - \sigma_{33})^2 + (\sigma_{33} - \sigma_{11})^2\right] + \sigma_{12}^2 + \sigma_{23}^2 + \sigma_{31}^2 \tag{C.8}$$

$$J_3 = \frac{2}{27}I_1^3 - \frac{1}{3}I_1 I_2 + I_3 \tag{C.9}$$

As a 2D plane strain case is studied, most components of the third dimension can be omitted, resulting in the following equations:

$$I_1 = \sigma_{11} + \sigma_{22} + \sigma_{33} \tag{C.10}$$

$$I_2 = \sigma_{11}\sigma_{22} + \sigma_{22}\sigma_{33} + \sigma_{33}\sigma_{11} - \sigma_{12}^2 \tag{C.11}$$

$$I_3 = \sigma_{11}\sigma_{22}\sigma_{33} \tag{C.12}$$

$$J_1 = 0 \tag{C.13}$$

$$J_2 = \frac{1}{3}I_1^2 - I_2 = \frac{1}{6}\left[(\sigma_{11} - \sigma_{22})^2 + \sigma_{22}^2 + -\sigma_{11}^2\right] + \sigma_{12}^2 \tag{C.14}$$

$$J_3 = \frac{2}{27}I_1^3 - \frac{1}{3}I_1 I_2 + I_3 \tag{C.15}$$

From this formulation it is clear that the deviatoric stress invariants can be calculated directly from the normal stress invariants. The main advantage of using stress invariants is that they do not change with rotation of the specimen. Therefore, it does not matter how a particular layer is oriented, because for each orientation the stress invariants are similar. In continuum mechanics this is often used to ignore the importance of orientation of the specimen.

D
Lode Angle

The definition of Lode angle used in this study is "the smallest angle between the line of pure shear and the projection of the stress tensor on the deviatoric plane" (Malcher and Andrade (2012)). The Lode Angle denoted by 'θ' is described as follows using two stress invariants J_2 & J_3:

$$\theta = \frac{1}{3}cos^{-1}\left(\frac{-\sqrt{27}J_3}{2J_2^{1.5}}\right) \tag{D.1}$$

The Lode angle can be used roughly to determine what kind of deformation is taking place at a particular point in the control volume. There are three different options:

Table D.1: Deformation types

	Behaviour
θ 0°	Extension
θ 30°	Shear
θ 60°	Compression

E

Determination of Material Parameters

This section covers all the 18 material parameters used in the elasto-viscoplastic model. Most can be determined by conducting laboratory experiments. However, to date, not all tests necessary to determine all parameters are performed on the same rock salt sample. Therefore, it was decided to use the values of the parameters discussed by Khaledi and Mahmoudi (2016a), as this paper provides a complete overview of all parameters. Most of the parameter values obtained from this article are consistent with the values found in the papers proposing the model Desai and Zhang (1987), Desai and Salami (1987), Desai and Varadarajan (1987). For some parameters, the laboratory experiments were already performed before the papers with the model proposed by Desai. In that case, reference is made to the original documents which further describe the test procedure. Next, all input parameters are discussed.

Density (ρ_{halite}, ρ_{litho}):

In this study two different densities are applicable, namely the density of rock salt ($\rho_{\text{halite}} = 2160\ \frac{kg}{m^3}$) and the density of the overburden ($\rho_{\text{litho}} = 2160\ \frac{kg}{m^3}$). It is assumed that the rock salt is pure halite (homogeneous) and that the density remains constant (unless stated otherwise).

Elastic moduli (K_b, μ, ν, E):

Elastic moduli quantify how a material deforms elastically when a load is applied. The bulk modulus (K_b) measures the resistance against deformation due to uniform compression. The shear modulus (μ) defines the resistance against deformation due to shearing. To measure the stiffness of the material the Young's modulus (E) is used. The Poisson's ratio (ν) describes the strain in transversal direction. In the paper by Khaledi and Mahmoudi (2016a), they state that common values for the Young's modulus and Poisson's ratio of rock salt are $E = 25000$ MPa and $\nu = 0.27$, respectively. With this information, the bulk and shear modulus are $K = 18115$ MPa and $\mu = 9842$ MPa.

Tensile rock strength (σ_t):

To account for cohesion, the tensile strength of salt is taken into account by transforming the stress coordinates (adding three times the tensile strength to the first stress invariant). The tensile strength of the rock can be determined by performing uniaxial tests, according to Kim and Lade (1984), rock salt has a tensile strength of 1.8 MPa.

Fluidity Parameters (μ_1, N_1):

The fluidity parameter, μ_1, and the exponent of the flow rule, N_1, are related to the rate-dependent behaviour of rock salt. Hansen (1978) and Herrmann and Wawersik (1980) performed creep tests on different rock salt samples to determine these parameters. The rock salt sample studied in Desai's work had similar properties and therefore he adopted the following values; μ_1 = $5.06 \cdot 10^{-7}$ day^{-1} and N_1 = 3. Later, the values for these parameters became common.

Viscoplastic Material Parameters (β, β_1, γ, m_v, n):

The first four parameters, β (-), β_1 (MPa^{-1}), γ (-) and m_v (-), are associated with the failure boundary of rock salt. These can be determined by performing triaxial tests and applying curve fitting techniques as described in Desai and Varadarajan (1987). For the sake of simplicity, it is often assumed that these parameters are constant. The coefficient n is related to the phase change point which indicates zero-volume change depending on the initial density and confinement of the material. Therefore, it can also be assumed that this parameter is constant according to Desai and Zhang (1987).

Table E.1: Viscoplastic material parameters from Desai and Zhang (1987).

	Value
β	0.995 (-)
β_1	4.8e-3 (MPa^{-1})
γ	0.11 (-)
m_v	-0.5 (-)
n	3 (-)

Hardening Parameters (α_1, α_0, η, k):

Four different hardening parameters are used to describe the hardening behaviour of the material. To describe the growth function (α), two hardening constants α_1 (MPa^{-1}) and η (-) respectively are needed. The values used in this study were originally determined by line fitting by Katona and Mulert (1984). To apply the non-associative flow rule, which distinguishes between the yield formulation and the potential function, two more constants are considered α_0 and k. The first, α_0, is a reference value equal to one stress unit (1 MPa). Parameter k can be a constant value or a stress dependent function, Desai and Zhang (1987) states that for rock salt the variation between rock salt samples is very insignificant and therefore assumes a constant of 0.275.

Table E.2: Hardening parameters from Katona and Mulert (1984).

	Value
α_1	0.00005 (MPa^{-1})
α_0	1 (MPa)
η	0.7 (-)
k	0.275 (-)

F

Detailed Description of Boundary Conditions

This section describes the boundary conditions for the simple box case and the boundary conditions for the EPE-S43 natural mesh case. First, a figure representing the mesh is given, followed by a brief description of the boundary conditions. A similar format to the the main section is used for the left corner point. In each case the left corner point has the most negative coordinates (i.e. (-1000, -1000) or (-150, -150)).

Boundary Conditions: Box Case Compression

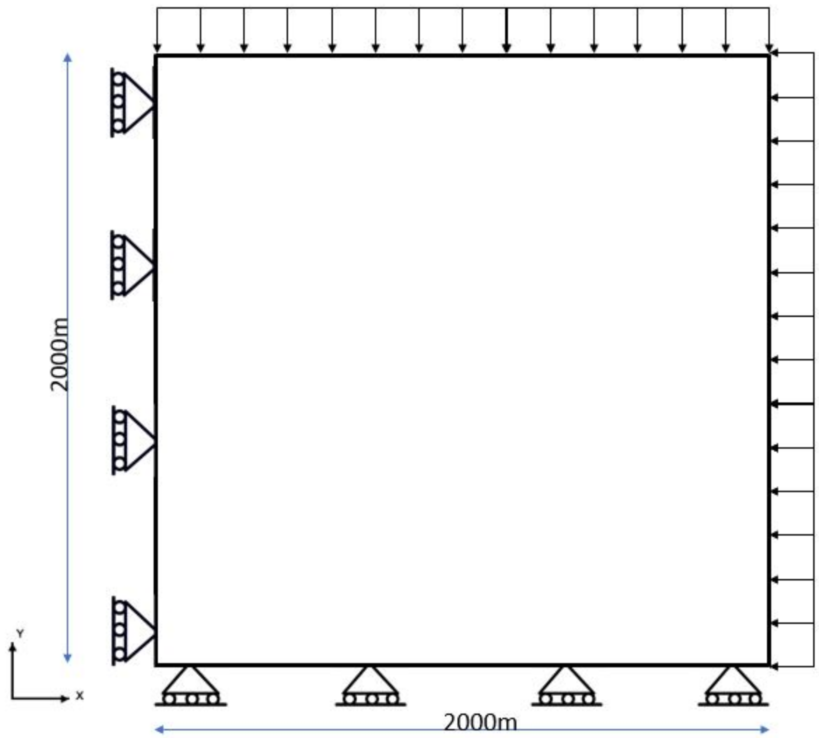

Figure F.1: Boundary Conditions for box case.

$$\text{Boundary Condition:} = \begin{cases} F_y = -5 \cdot 10^6 N & \text{at } y = 1000, -1000 < x < 1000 \\ F_x = -5 \cdot 10^6 N & \text{at } -1000 < y < 1000, x = 1000 \\ u_x = 0 & \text{at } -1000 < y < 1000, x = -1000 \\ u_y = 0 & \text{at } y = -1000, -1000 < x < 1000 \end{cases} \tag{F.1}$$

$$\text{Initial Condition:} = \begin{cases} \sigma_{xx} = \sigma_{yy} = \sigma_{zz} = 0 & \text{at } -1000 < y < 1000, -1000 < x < 1000 \\ u_x = u_y = 0 & \text{at } -1000 < y < 1000, -1000 < x < 1000 \end{cases} \tag{F.2}$$

Boundary Conditions: Cylindrical Cavern Case

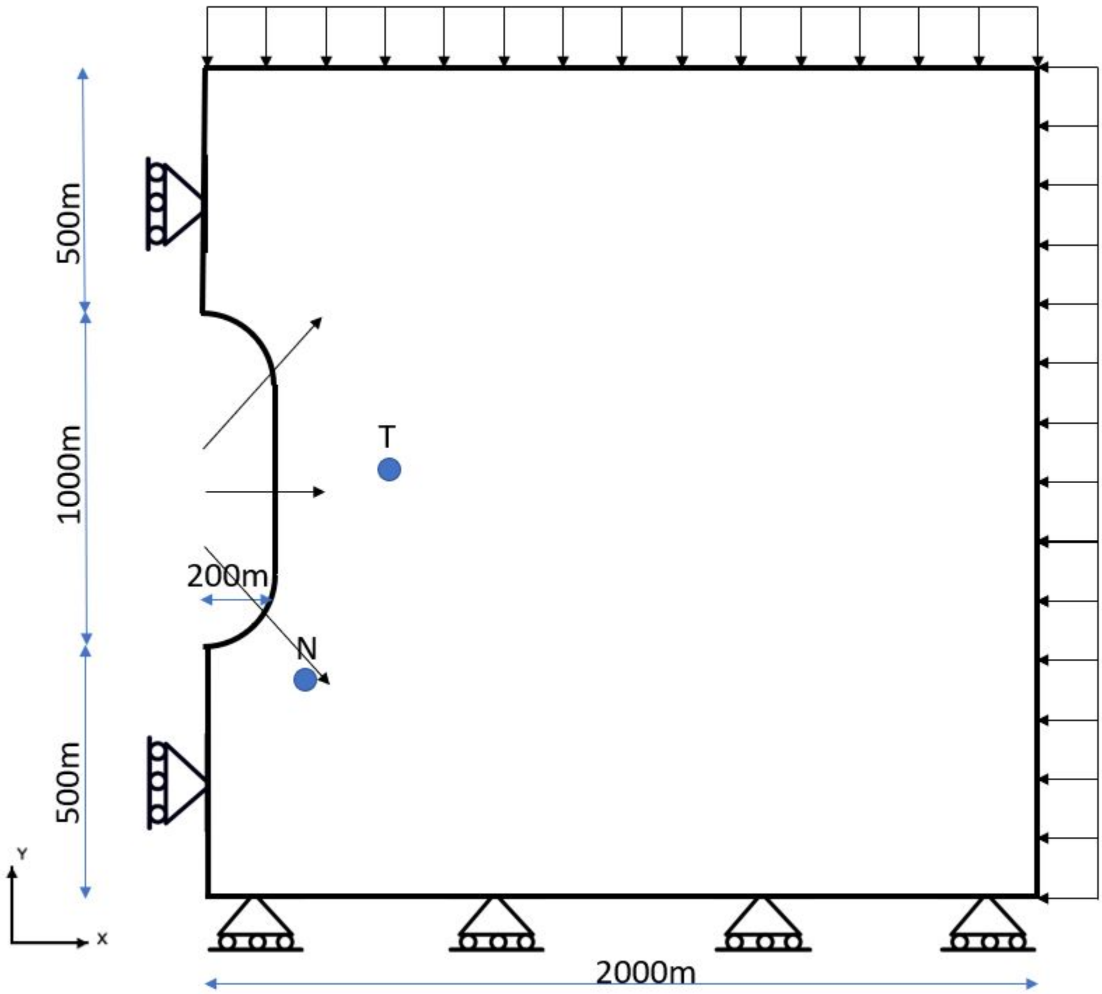

Figure F.2: Boundary Conditions for the cylidrical cavern case including two reference points denoted by N and T.

$$\text{Boundary Condition:} = \begin{cases} F_y = P_c \cdot sin(\alpha) \cdot l \cdot w & \text{at } -500 < y < 500, -1000 < x < -800 \\ F_x = P_c \cdot cos(\alpha) \cdot l \cdot w & \text{at } -500 < y < 500, -1000 < x < -800 \\ u_x = 0 & \text{at } -1000 < y < 1000, x = -1000 \\ u_y = 0 & \text{at } y = -1000, -1000 < x < 1000 \end{cases} \tag{F.3}$$

$$\text{Initial Condition:} = \begin{cases} \sigma_{xx} = \sigma_{yy} = \sigma_{zz} = \sigma_v & \text{at } -1000 < y < 1000, -1000 < x < 1000 \\ u_x = u_y = 0 & \text{at } -1000 < y < 1000, -1000 < x < 1000 \end{cases} \tag{F.4}$$

Boundary Conditions: Real Cavern Case

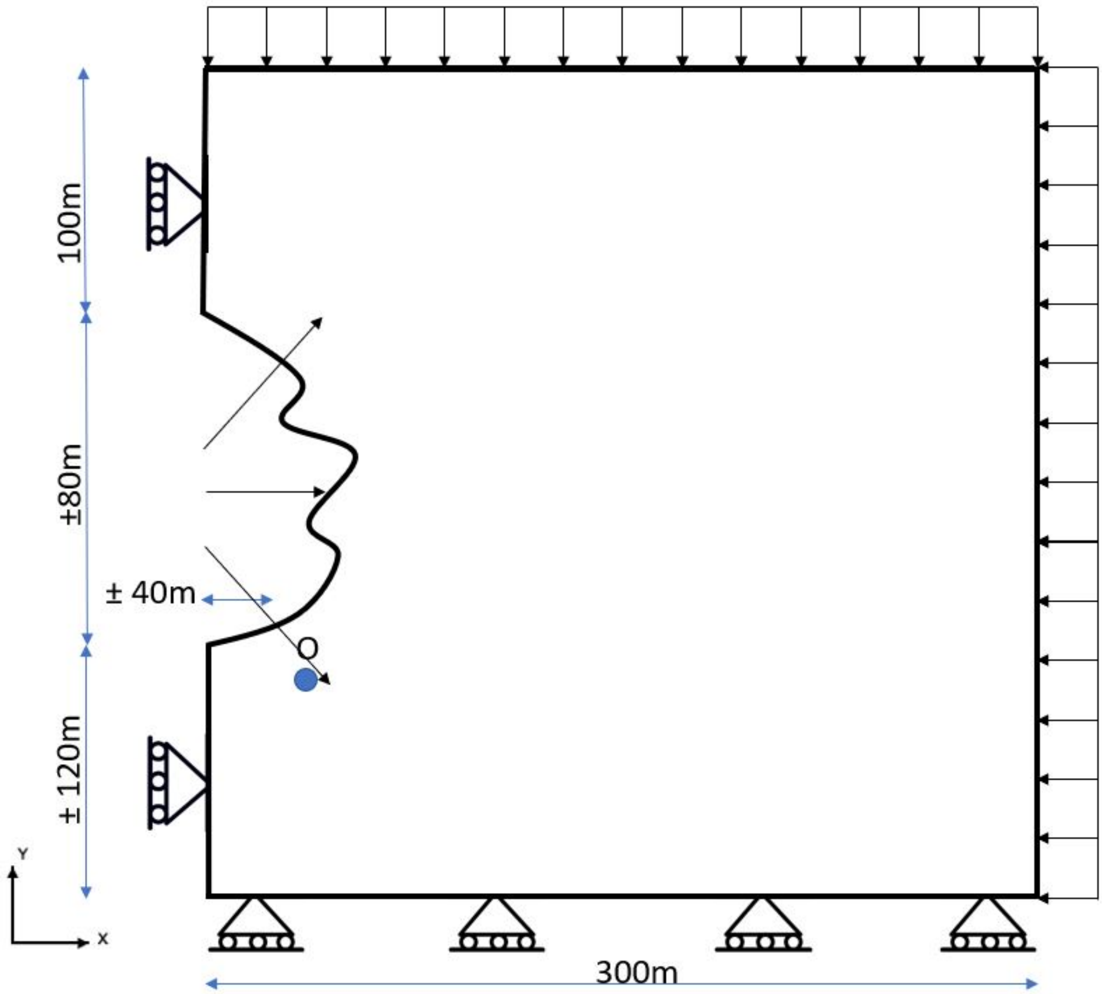

Figure F.3: Boundary Conditions EPE S43 cavern including one reference point O.

$$\text{Boundary Condition:} = \begin{cases} F_y = P_c \cdot sin(\alpha) \cdot l \cdot w & \text{at } -30 < y < 50, -150 < x < -110 \\ F_x = P_c \cdot cos(\alpha) \cdot l \cdot w & \text{at } -30 < y < 50, -150 < x < -110 \\ u_x = 0 & \text{at } -150 < y < 150, x = -150 \\ u_y = 0 & \text{at } y = -150, -150 < x < 150 \end{cases} \tag{F.5}$$

$$\text{Initial Condition:} = \begin{cases} \sigma_{xx} = \sigma_{yy} = \sigma_{zz} = \sigma_v & \text{at } -150 < y < 150, -150 < x < 150 \\ u_x = u_y = 0 & \text{at } -150 < y < 150, -150 < x < 150 \end{cases} \tag{F.6}$$

where P_c is the cavern pressure, α the inclination angle, l and w the dimensions of the element and σ_v the confining pressure.

G
Results: Box Case

The results for displacement, strain and stress in the x and y directions are displayed in figure G.1. In short, when a negative force is applied to both the top and right surfaces, one would expect a smoothly decreasing displacement field from the boundaries at which the forces are applied. The surfaces on which the forces are exerted have the largest displacement and due to the boundary conditions applied the displacement is zero at both the left and the bottom. Stress and strain can be calculated directly from displacement by using a strain-displacement relationship (eq.2.4) and Hooke's law (eq.2.7). So if the displacement in both x and y directions decrease linearly across the mesh, stress and strain will be constant. Since the two applied forces are equal, so is the response in both directions. This is visible in the figure below. One note is that the stress and strain are **not** exactly constant due to the error caused by using a numerical approximation to obtain the solution (differences in solution are on the order of 10^{-12}).

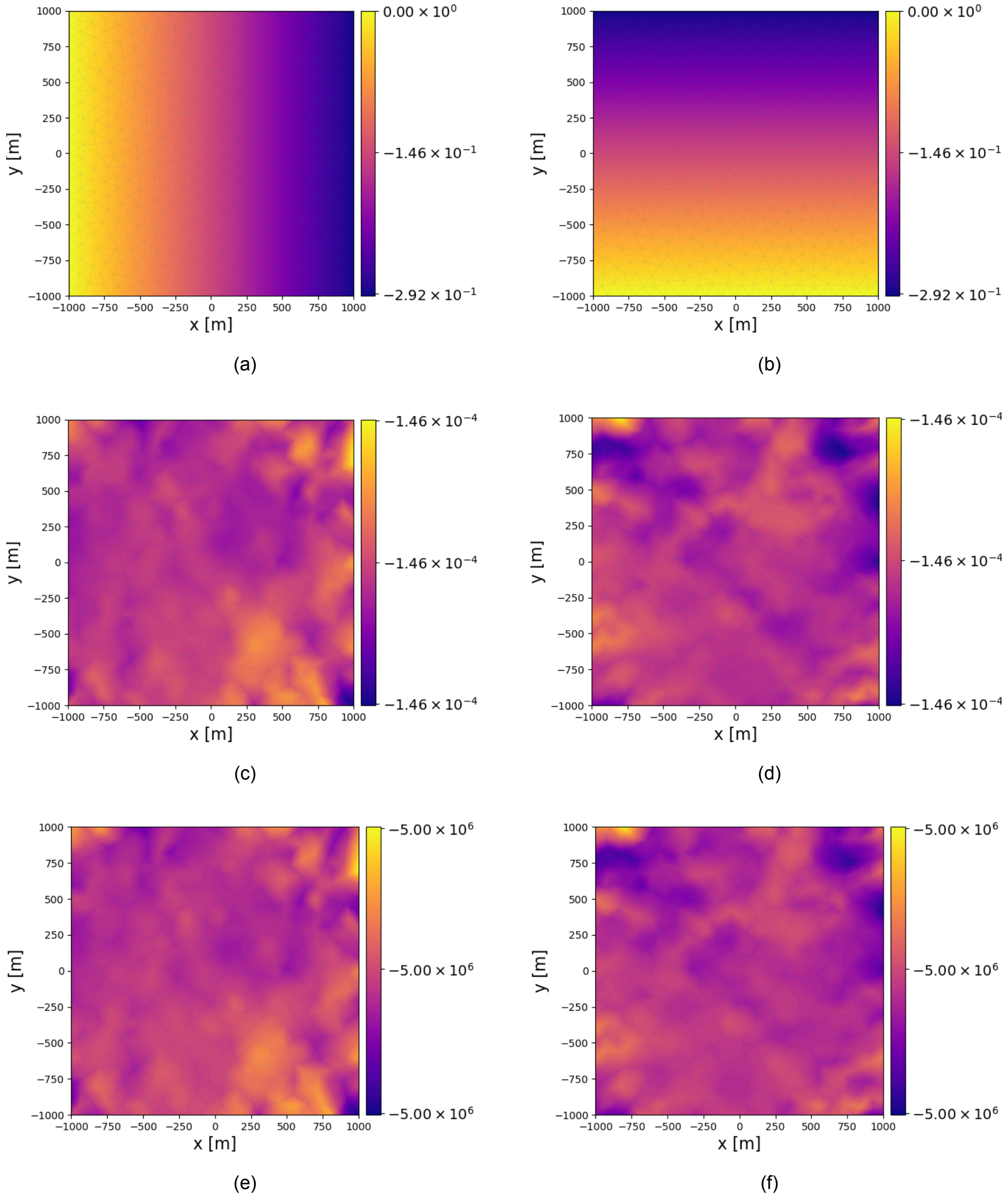

Figure G.1: Summary of the results for box case. (a) Displacement in x-direction; (b) Displacement in y-direction; (c) Strain in x-direction; (d) Strain in y-direction; (e) Stress in x-direction; (f) Stress in y-direction

H

Meshes for Consistency Analysis

The meshes used for the consistency analysis and differences for the most refined mesh are displayed in this appendix. The difference between the numerical and analytical solutions of the elastic predictor model is calculated on these meshes. Each refinement divides each element in half.

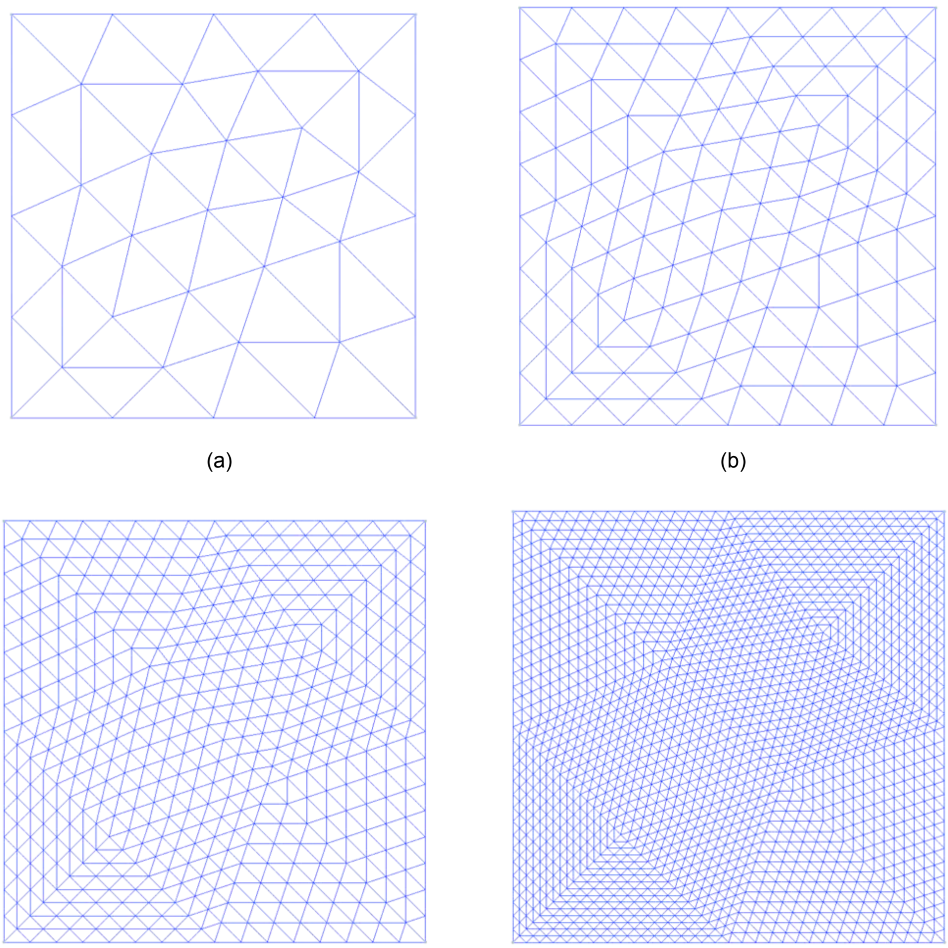

(a) (b) (c) (d)

Figure H.1: Meshes used for consistency analysis (a) 56 elements; (b) 224 elements; (c) 896 elements; (d) 3584 elements

In the next two figures the numerical and analytical solution and their differences are presented, these solutions are results for the most refined mesh consisting of 3584 elements.

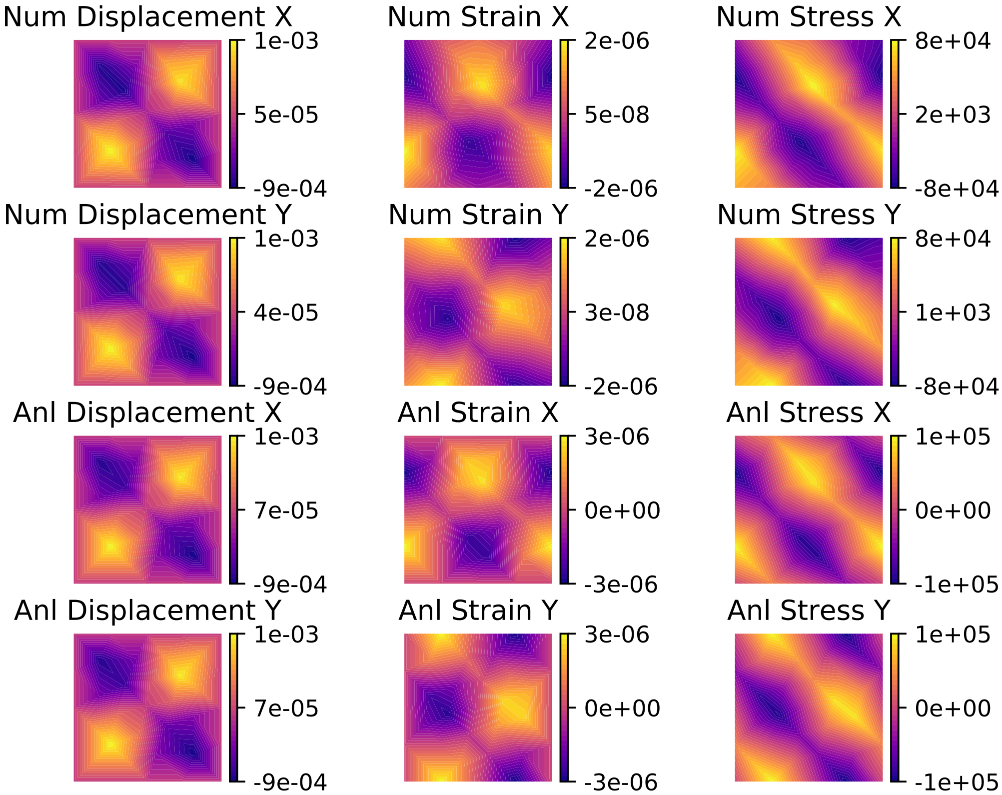

Figure H.2: Analytical and numerical solution for displacement, stress and strain in x and y direction for 3584 elements.

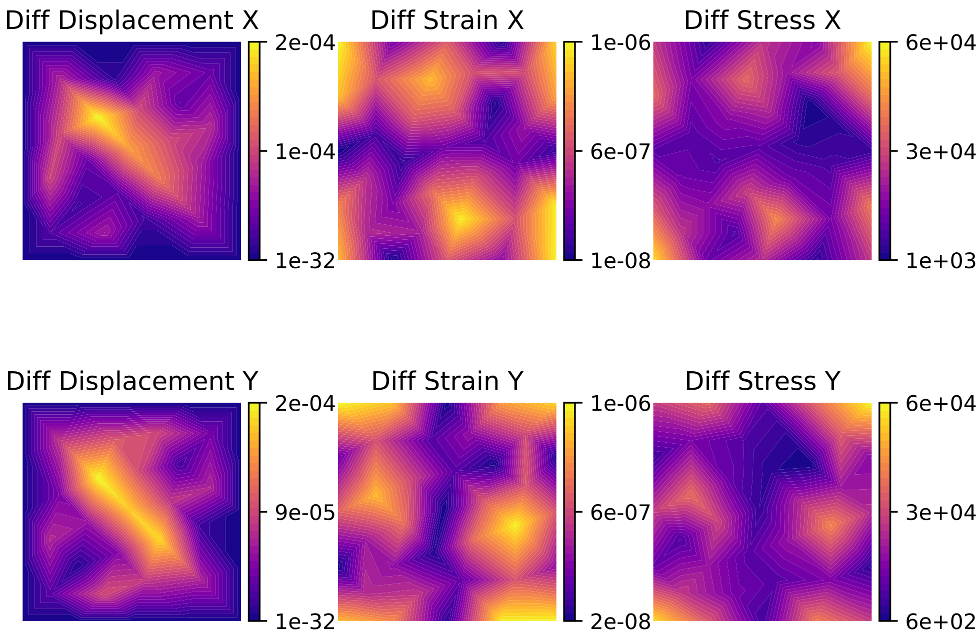

Figure H.3: Differences between analytical and numerical solution for 3584 elements.

EPE S43

This chapter contains all additional information for the natural cavern mesh application of EPE-S43. The information about the cavern is taken from Laban (2020). The sonar measurements are displayed first, then the corresponding meshes created are shown. Finally, the results for the other three meshes are displayed (67L, 85R & 85L).

Sonar Measurements

Since the available data are 2D cross sections, it was decided to create four meshes, one in each direction (north, east, south and west). The two sonar data figures are cut in half, creating a total of four meshes. The names of these meshes correspond to the side on the sonar data.

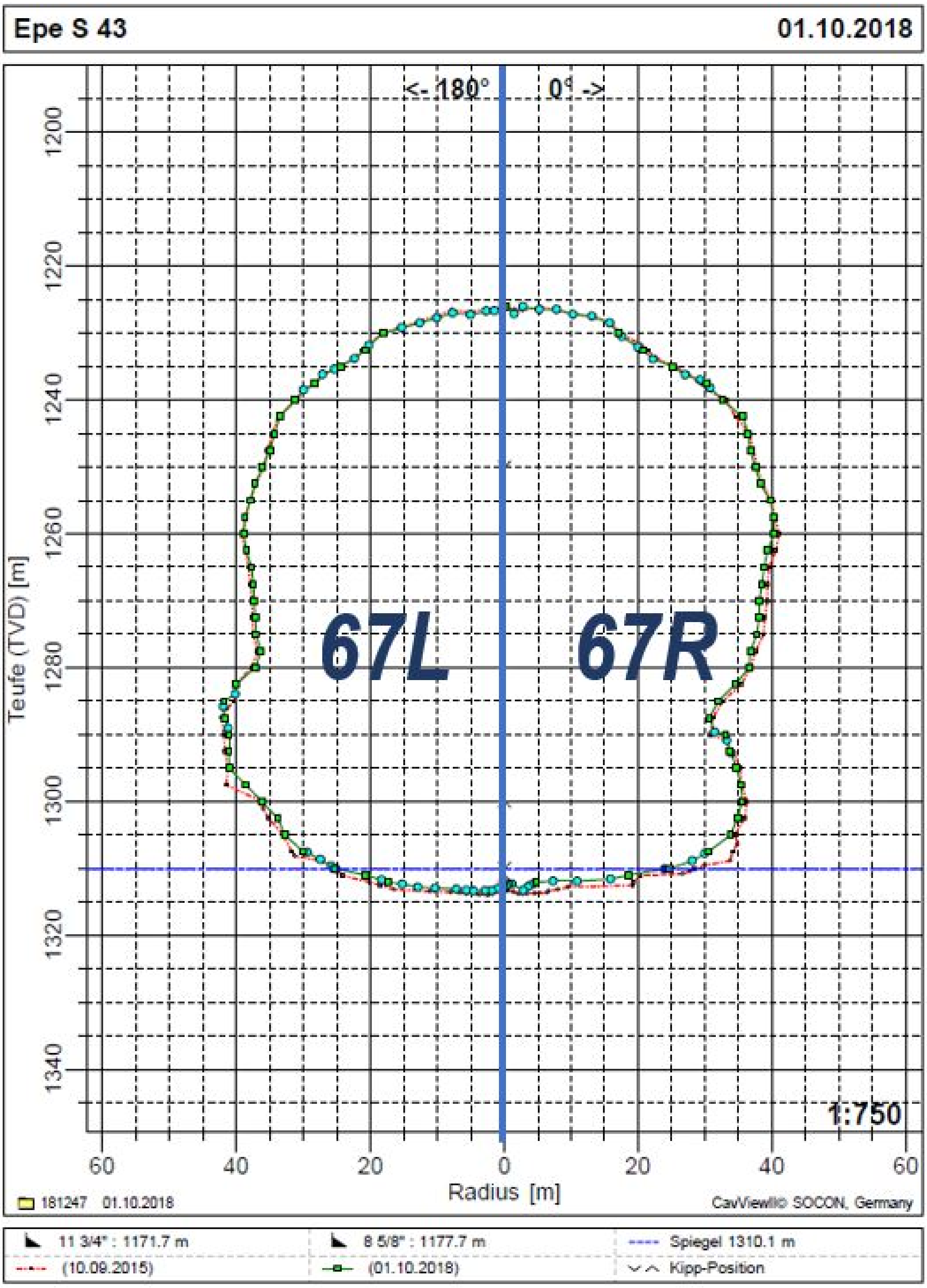

Figure I.1: Sonar Data for mesh 67L and 67R.

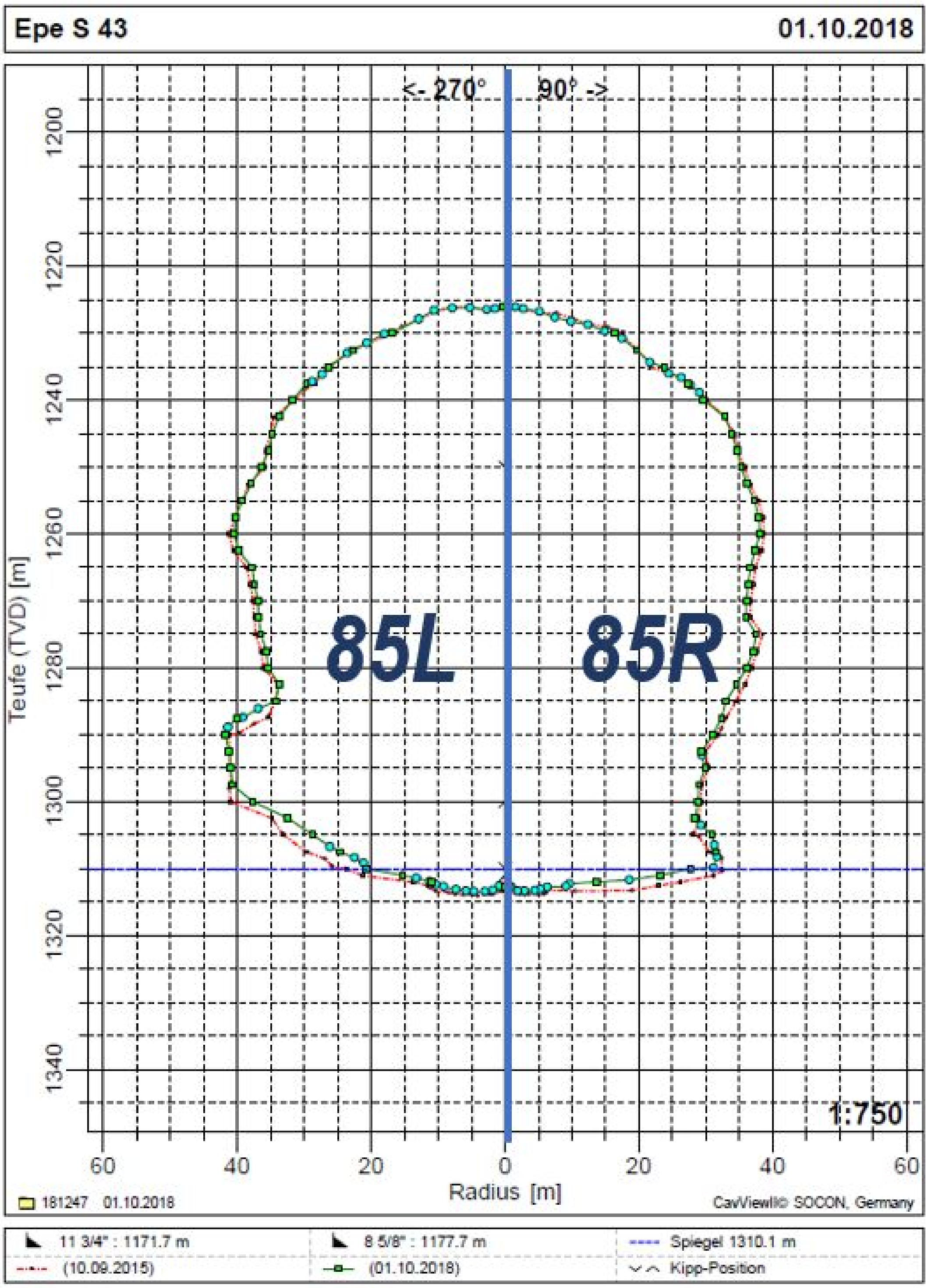

Figure I.2: Sonar Data for mesh 85L and 85R.

Meshes

Next, the four meshes describing the previously mentioned sonar data are displayed. These meshes were created using the open source GMSH software.

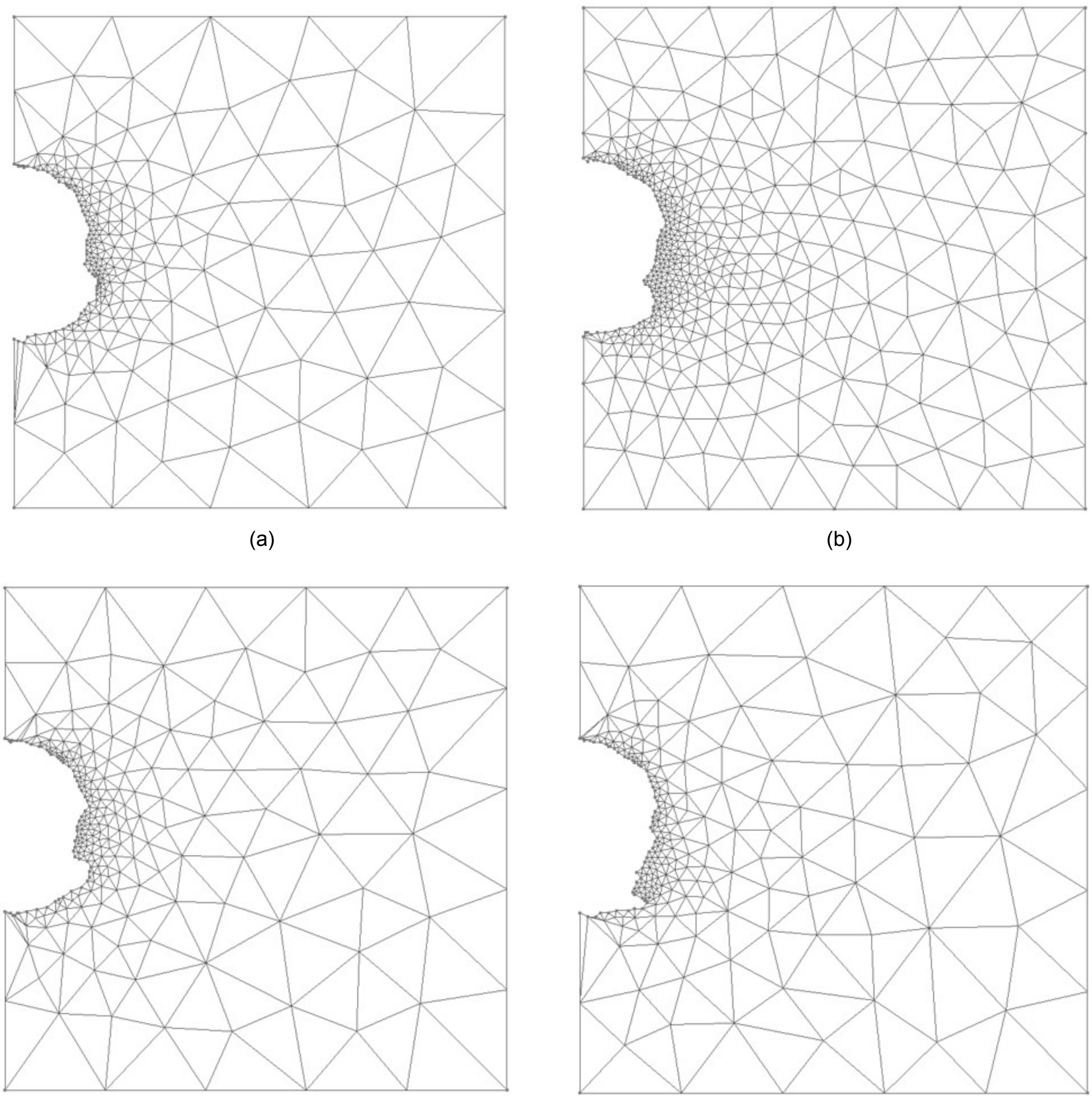

(a) (b) (c) (d)

Figure I.3: Meshes used for EPE S43 cavern (a) Mesh 67L; (b) Mesh 67R; (c) Mesh 85L; (d) Mesh 85R

Results for Mesh 67R

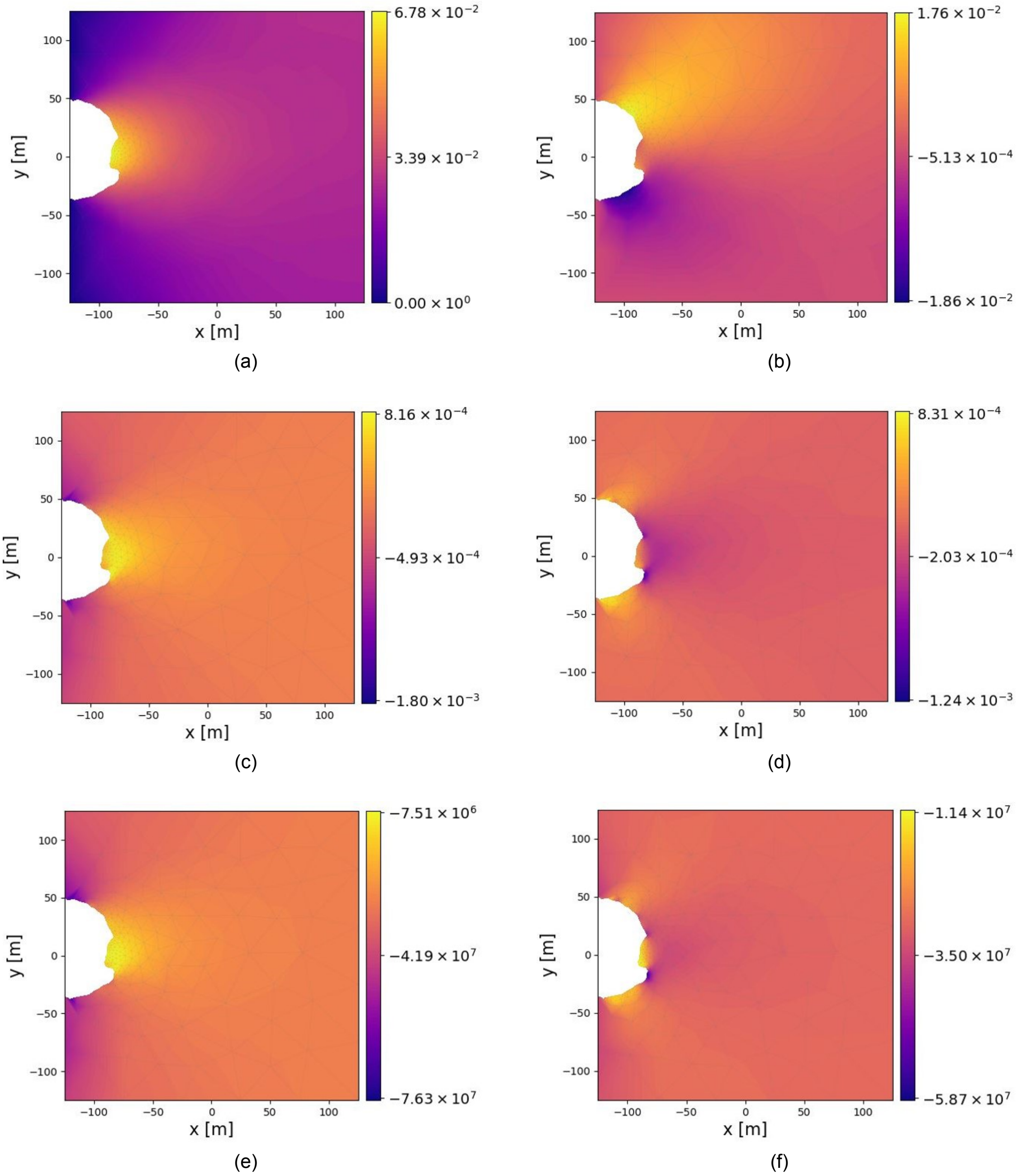

Figure I.4: Elasto-viscoplastic response of mesh 67R at 21 MPa for (a) displacement in x-direction (m); (b) displacement in y-direction (m); (c) strain in x-direction; (d) strain in y-direction; (e) stress in x-direction (Pa); (f) stress in y-direction (Pa).

Results for Mesh 85L

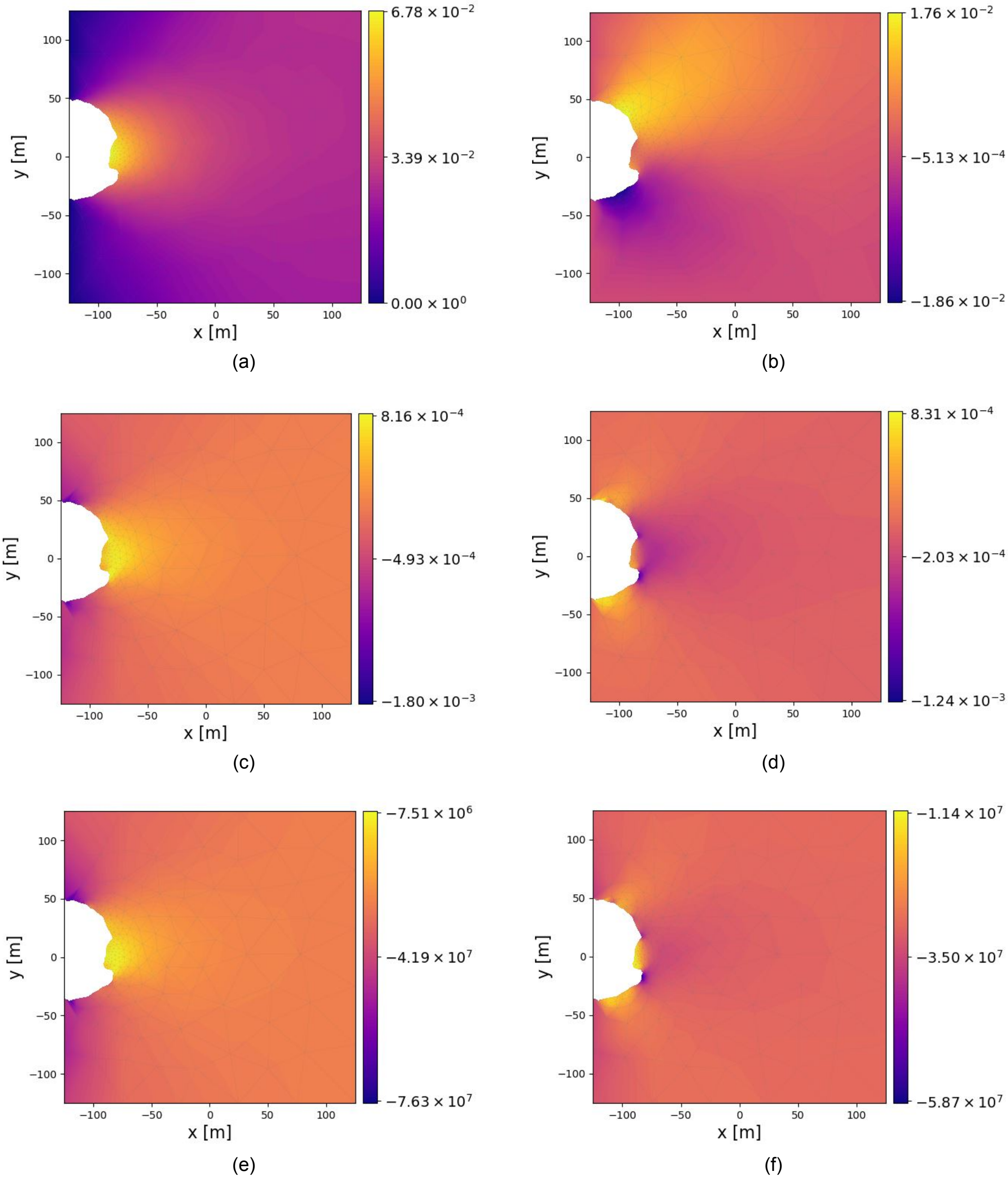

Figure I.5: Elasto-viscoplastic response of mesh 85L at 21 MPa for (a) displacement in x-direction (m); (b) displacement in y-direction (m); (c) strain in x-direction; (d) strain in y-direction; (e) stress in x-direction (Pa); (f) stress in y-direction (Pa).

Results for Mesh 85R

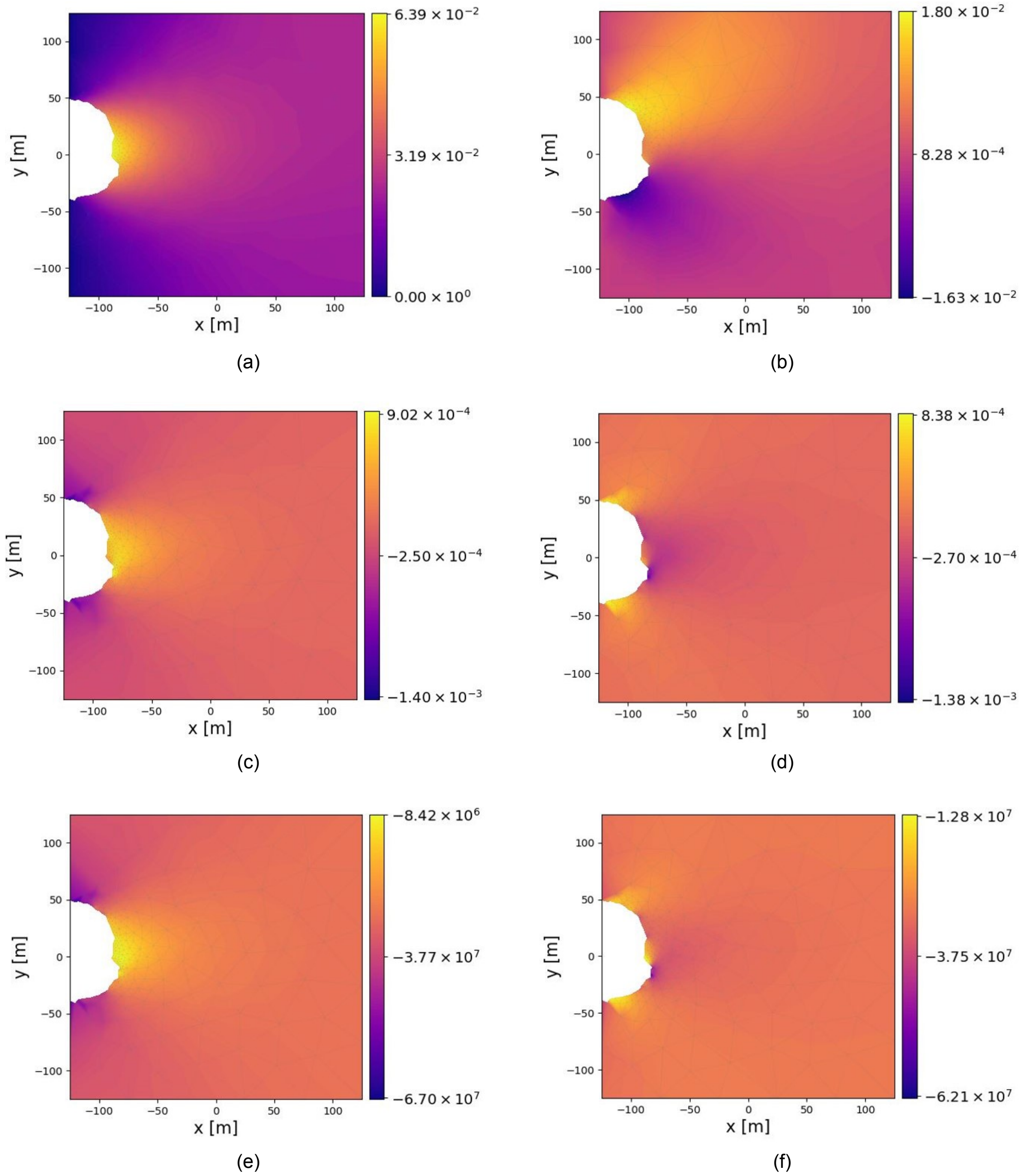

Figure I.6: Elasto-viscoplastic response of mesh 85R at 21 MPa for (a) displacement in x-direction (m); (b) displacement in y-direction (m); (c) strain in x-direction; (d) strain in y-direction; (e) stress in x-direction (Pa); (f) stress in y-direction (Pa).

Bibliography

G. Y. Baladi and B. Rohani. An elastic-viscoplastic constitutive model for earth materials. U.S. Army Engineer Waterways Experiment Station, 1983.

R. B. J. Brinkgeve. Plasticity theory and failure criteria (cie4361). *TU Delft*, pages 1–224, 2019.

P. Bérest. *Mechanical Behaviour of Salt VII*. CRC Press, 2012.

D. G. Caglayan and N. Weber. Technical potential of salt caverns for hydrogen storage in europe. *International Journal of Hydrogen Energy*, 45(11):6793–6805, 2020. doi: 10.1016/j.ijhydene.2019.12.161.

I. C. Cormeau and O. C. Zienkiewicz. Visco-plasticity and plasticity an alternative for finite element solution of material nonlinearities. *Computing Methods in Applied Sciences and Engineering*, 10(1): 821–845, 2005.

C. Desai and L. Laloui. Disturbed state concept for partially saturated soils. *Numerical Models in Geomechanics - NUMOG*, pages 129–133, 1997.

C. S. Desai. A general basis for yield, failure and potential functions in plasticity. *International Journal for Numerical and Analytical Methods in Geomechanics*, 4(4):361–375, 1980. doi: 10.1002/nag.1610040406.

C. S. Desai and S. K. Pradhan. Dsc model for soil and interface including liquefaction and prediction of centrifuge test. *Journal of Geotechnical and Geoenvironmental Engineering*, 2(132), 2006. doi: 10.1061/ASCE1090-02412006132:2214.

C. S. Desai and M. R. Salami. A constitutive model and associated testing for soft rock. *International Journal of Rock Mechanics & Mining Sciences*, 24(5):299–307, 1987. doi: 10.1016/0148-9062(87)90866-7.

C. S. Desai and A. Varadarajan. A constitutive model for quasi-static behaviour of rock salt. *Journal of Geophysical Research*, 92(11):11–43, 1987. doi: 10.1029/JB092iB11p11445.

C. S. Desai and D. Zhang. Viscoplastic model for geological materials with generalized flow rule. *International Journal For Numerical and Analytical Methods in Geomechanics*, 11(6):603–620, 1987. doi: 10.1002/nag.1610110606.

EBN. Energy in the netherlands, 2018. URL https://www.ebn.nl/wp-content/uploads/2018/04/EBN-poster-numbers2016.pdf.

M. O. Faruque. Implementation of a general constitutive model for geological materials. *International Journal for Numerical and Analytical Methods in Geomechanics*, 9(5):415–436, 1985. doi: 10.1002/nag.1610090503.

C. Geuzaine and J. F. Remacle. Gmsh: a three-dimensional finite element mesh generator with built-in pre- and post-processing facilities. *International Journal for Numerical Methods in Engineering*, 79 (11):1309–1331, 2009. doi: 10.1002/nme.2579.

F. D. Hansen. Quasi-static strength and creep deformational characteristics of bedded salt from the carey mine near lyons, kansas. United States Government, 1978.

W. Herrmann and W. D. Wawersik. Analysis of steady state creep of southeastern new mexico bedded salt. United States Government, 1980.

G. Hévin. Underground storage of hydrogen in salt caverns. *European workshop on underground energy storage*, 2019.

J. Juez-Larré and S. van Gessel. Assessment of underground energy storage potential to support the energy transition in the netherlands. *First Break*, 37(7):57–66, 2019.

A. Kabuth and A. Dahmke. Energy storage in the geological subsurface: dimensioning, risk analysis and spatial planning: the angus+ project. *Environmental Earth Sciences*, 76(23):86–104, 2017. doi: 10.1007/s12665-016-6319-5.

M. G. Katona and M. A. Mulert. A viscoplastic cap model for soils and rocks. *Journal of Geotechnical Engineering*, 110(8):1–20, 1984. doi: 10.1061/(ASCE)0733-9410(1984)110:8(1106).

K. Khaledi. Constitutive modeling of rock salt with application to energy storage caverns. Civil and Environmental Engineering Rurh-Universität Bochum, 2017.

K. Khaledi and A. Mahmoudi. Stability and serviceability of underground energy storage caverns in rock salt subjected to mechanical cyclic loading. *International Journal of Rock Mechanics & Mining Sciences*, 86:115–131, 2016a. doi: 10.1016/j.ijmms.2016.04.010.

K. Khaledi and E. Mahmoudi. Analysis of compressed air storage caverns in rock salt considering thermo-mechanical cyclic loading. *Environmental Earth Sciences*, 75(1149):15–31, 2016b. doi: DOI10.1007/s12665-016-5970-1.

M. K. Kim and P. V. Lade. Modelling rock strength in three dimensions. *International Journal of Rock Mechanics and Mining Sciences & Geomechanics Abstracts*, 21(1):21–33, 1984. doi: 10.1016/0148-9062(84)90006-8.

K. Krabbenhoft. Basic computational plasticity. Department of Civil Engineering; Technical University of Denmark, 2002.

M. Laban. Hydrogen storage in salt caverns: Chemical modelling and analysis of large-scale hydrogen storage in underground salt caverns. *Delft University of Technology*, 2020.

A. Makhmutov. Nonlinear 2d finite element modeling: Cyclic energy storage in salt caverns with creep deformation physics. *Delft University of Technology*, 2020.

L. Malcher and F. M. Andrade. An assessment of isotropic constitutive models for ductile fracture under high and low stress triaxiality. *International Journal of Plasticity*, 30(1):81–115, 2012. doi: 10.1016/j.ijplas.2011.10.005.

W. D. Pepper and J. C. Heinrich. *The Finite Element Method: basic concepts and applications with MATLAB, MAPLE, and COMSOL*. CRC Press, 2017.

P. Perzyna. Fundamental problems in viscoplasticity. *Advanced in Applied Mechanics*, 9(3):243–377, 1966. doi: 10.1016/S0065-2156(08)70009-7.

S. S. Rao. *The Finite Element Method in Engineering*. Elsevier, 2005.

O. C. Zienkiewicz and I. C. Cormeau. Visco-plasticity - plasticity and creep in elastic solids - a unified numerical solution approach. *International Journal For Numerical Methods In Engineering*, 8(23): 821–845, 1974. doi: 10.1002/nme.1620080411.